ADVANCED SUN-SENSOR PROCESSING AND DESIGN FOR SUPER-RESOLUTION PERFORMANCE

by

Godard

B.Eng - Aerospace Engineering
Ryerson University, 2004

A thesis

presented to Ryerson University

in partial fulfillment of the requirements for the degree of

Master of Applied Science

In the program of

Mechanical Engineering

Toronto, Ontario, Canada 2006

AUTHOR'S DECLARATION

I hereby declare that I am the sole author of this thesis

I authorize Ryerson University to lend this thesis to other institutions or individuals for the purpose of scholarly research.

17 MAY 2006

I further authorize Ryerson University to reproduce this thesis by photocopying or by other means, in total or in part, at the request of other institutions or individuals for the purpose of scholarly research.

17 MAY 2006

ABSTRACT

Advanced Sun-Sensor Processing and Design for Super-Resolution Performance

Master of Applied Science 2006, Godard

School of Graduate Studies, Ryerson University

The performance of conventional and parametric super-resolution algorithms for estimating sun position in a spacecraft sun-sensor was analyzed. Widely employed in other applications, parametric algorithms were examined to evaluate increase in system performance without affecting the cost of the sensor system. Using a simplified model of detector illumination simulations provided quantitative comparisons of algorithm performance. Simple sensor re-design was examined by using genetic algorithms as a heuristic to optimize the illumination pattern for a single axis digital sun-sensor. Findings show that, multiple narrow peak patterns provide subpixel accuracy in resolving the sun-angle. The optimal illumination pattern can be implemented by fabricating a replacement aperture mask for the sensor and this change can be made at a minimal cost. The super-resolution algorithms were tested with a component noise model and image degradation due to Earth albedo effects were examined. Parametric algorithms display very good performance throughout the test regime. The improvements are substantial enough to validate this approach worthy of future study.

ACKNOWLEDGMENTS

I would like to thank my thesis supervisor Dr. John Enright for granting me the opportunity to work on this topic. Most importantly, he has been my mentor for the last two years, giving advice and providing me with resources and encouragement to pursue my work.

A special thanks to Dr. Don McTavish, Dr. Jeffrey Yokota, and Dr. Galina Okouneva, who helped me to tackle a few hurdles during the course of my research.

My friends and family have been a constant source of support and inspiration. Special thanks to other two members of the AAG family - my best friends - Atif Mohammad and Ankit Garg. The basics of signal processing and certain areas of programming in MATLAB were taught by my friend Sajan Abdul. I woud like to thank Siddharta Bojje for letting me stay over at his place when I worked late in my lab during the nights and giving me the encouragement to move further ahead with aerospace research. The long and never ending time in the lab was made bearable by my friend Kamran Shahid. He is one person who kept giving me hope that this work will be done on time.

Simply I could not have reached here where I am today without my Father Dr. T.P. Nazar, my Mother Dr. Ramla Nazar, and my Brother T.P. Fellini. Last, but certainly not the least, I would like to thank my darling Azra Khayum. Thank you for your love and support without which I would have had a hard time completing this work. I dedicate this work to you, and for you I continue to exist.

DEDICATION

This thesis is dedicated to my parents who have given me all the support I needed:

Dr. T.P. Nazar and Dr. Ramla Nazar

TABLE OF CONTENTS

LIST OF TABLES

LIST OF FIGURES

NOMENCLATURE

τ	linear displacement
w	width of the slit [mm]
c	constant
$x(t)$	continuous signal
$x[n]$	discrete signal
$E\{\}$	expected value
N_F	fresnel number
i	current [A]
M,m	mass [kg]
V_e	volts [V]
ΔX	pixel spacing
$I(x,y)$	position in a 2-D image
λ	wavelength (nm)
n_{glass}	index of refraction
z_s	filter thickness
$w[n]$	noise process
σ_n^2	variance
μ	mean
$(\,)^H$	conjugate transpose
$(\,)^*$	complex conjugate
$\hat{(\,)}$	estimate

Chapter 1

INTRODUCTION

Sun-sensors represent an essential component of the attitude control systems on modern spacecraft. These compact, low-power devices provide coarse- to medium- resolution measurements of the spacecraft's attitude with respect to the sun. Due to their low cost, low mass, and low power-consumption, multiple units are frequently employed to give 4π-steradian coverage around the satellite. These same characteristics allow these sensors to be widely deployed in different classes of missions from nano-satellites of a few kilograms to large missions of several tons. Many space-hardware manufacturers have recently introduced new models of sun-sensors, however, the basic operation and processing of these devices has not changed substantially in the last thirty years.

Innovative microsatellite designs have pioneered many advances in satellite technology. Therefore, there is an increasing demand for performance and capability of attitude sensors onboard microsatellites. The traditional high-performance attitude control system (ACS) sensors are not affordable. The purpose of this research is to demonstrate that the performance of digital sun-sensors can be improved by,

1. Intelligent processing strategies that can extract information more efficiently from raw sensor data.
2. Simple low/no cost component changes to the sensor design that can yield substantial performance gains.

The recent flood of successful Commercial-Off-The-Shelf (COTS) component parts allows for rapid development of sensors that have low cost, low power consumption, and low mass, but they do not always provide the required performance. This study focuses on increasing the angular accuracy of digital sun-sensors by developing intelligent algorithms that can provide encouraging gains when compared to existing processing techniques. Other ways to re-design the sensor for increased performance can then be implemented based on the accuracy of the new processing routines.

1.1 Sun-Sensor Operation

Sun-sensors are the single most commonly used attitude acquisition sensors on modern spacecraft. A spacecraft's sun-sensors measure the relative angular position of the sun. The Sun is the most easily identified object in the spacecraft sky because its brightness makes it easy to distinguish it from other stellar objects. Therefore, it is an important aspect of the attitude determination and control (ADC) system onboard a spacecraft. Many sensor models exist: some sensors make only a single-angular measurement, others, two (e.g. azimuth and elevation). Rotations around the satellite-sun vector are not observable — to obtain three-axis attitude information, a spacecraft must use another type of navigation sensor.

Most sun-sensors share a common operating principle. Light from the sun strikes a patterned mask. Common mask elements are slits [Chen & Lerner, 1978] and pinholes [Liebe et al, 2002]. The patterned light which strikes the detector is first converted into an electric signal and then into an attitude reading after it is processed. Broadly speaking, sun-sensors come in two varieties: analog and digital.

1.1.1 Analog Sun-sensors

Analog sensors compare the variable output from a small number of photo-sensors to determine the sun angle. These devices are quite robust and can be calibrated to achieve good angular accuracy ($0.05°$) [Falbel & Paluszek, 2001]. Analog sensors generally display better angular accuracy than their digital counterparts, however, they are significantly affected by

stray light. Analog sensors, while very sensitive, operate by calculating the centroid of all the light passing through the optical mask. Thus, the presence of the earth or the moon in the field-of-view will distort the sun position estimate. If uncorrected, this can result in an error of up to 20° [Appel, 2003]. The impact of these effects can be reduced for spacecraft in sun-synchronous orbits with judicious placement of sensors and baffles, but arbitrary Earth-Sun-Spacecraft orientations remain problematic.

1.1.2 Digital Sun-sensors

Digital sensors replace the small number of photo-sensors with a linear or rectangular array of pixel sensors. The sensitivity of an individual pixel is less than that of an analog sensor, but a larger number of sensing regions improves the spatial selectivity of the device; each pixel only 'sees' a portion of the sky. One advantage of digital sensors is their relative immunity to effects of stray light. By implementing an active pixel array intead of solar cells, digital Sun-sensors are mostly insensitive to albedo light. Some configurations result in errors in the least significant bits of the digital Sun-sensors. The field-of-view of a single pixel on a digital sun-sensor is small, and the light intensity of the Sun is several orders higher (magnitude) than the intensity of the light reflected from the Earth. Hence, the reflected light does not deteriorate of measurement unlike in the case of analog sensors where the reflected light can be seen at very large field-of-view by a single photo-sensitve element. Since spatial selectivity is inherent in the pixel readout, once the sensor identifies those pixels that have no view of the sun, it can exclude those pixels from its attitude calculations. Thus, digital sensor performance is heavily influenced by the effectiveness of the sensor processing routines.

1.2 Array Processing and Super-Resolution

Although variations exist in detector technologies, most digital sensors operate in a similar manner. Each pixel in the sensor responds to the incoming radiative flux and produces an analog output proportional to the number of photons collected during a specific integration period. This value is proportional to the intensity of the irradiance observable by that pixel.

The analog intensity measurement is then converted to a digital value by using an analog-to-digital converter (ADC) integrated with the sensor array.

Most sensors display peak sensitivity in the visible spectrum and employ relatively coarse discretization (8-bit). Each pixel in the sensor array yields an intensity reading and the ensemble of the pixels in the array can be considered an *image*[1]. The processing algorithm for this sensor must then extract the sun-direction from the digitized image.

To be efficient, the processing algorithms must:

1. Identify the portion of the image illuminated by direct sunlight, and;
2. Associate that illumination with a specific part of the field of view.

The former point reflects the selectivity of an algorithm and, consequently, its resistance to stray light. The second, is a measure of its angular accuracy.

The above definition is purposefully oblique, however, a concrete example can provide a useful illustration. Rays traced from the sun passing through a narrow slit and then onto a linear array (Fig 1.1), will provide illumination over several pixels. Although geometric optics may not completely capture the optical behaviour of the device, it is clear that moving the sun within the field-of-view will illuminate different pixels on the sensor array.

Since each pixel responds to light originating from a restricted part of the sensor's field-of-view, there is an equivalence between isolating the sun's light to a single pixel and isolating the sun to a particular angular range of the field-of-view. The sensor's ability to locate the sun in the sensor image is directly related the accuracy of its sun-angle estimate. Although two-dimensional effects and sensor-geometry may complicate the relation to some degree, this basic reasoning still holds. The spacing between pixels and hence the spacing between the associated solid regions of the field-of-view defines the native resolution of the sensor.

1. Unless otherwise stated the term *image* will refer to the ensemble output of either a rectangular or linear array. Although, this is not strictly an image in the traditional sense, the nomenclature is convenient.

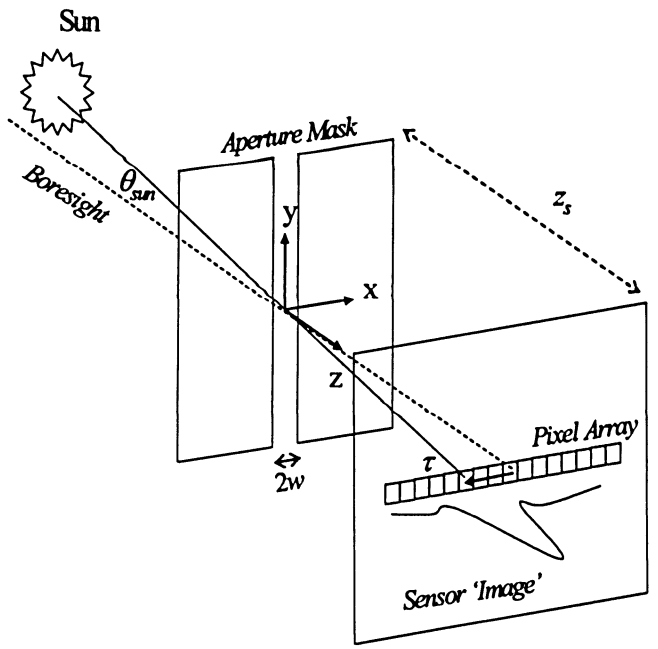

Figure 1.1 One Dimensional, Single Slit Sun-sensor. Spacing between the aperture mask and the array plane denoted z_s and slit half-width is w. Sensor geometry relates sun angle, θ_{sun}, to linear displacement, τ, of sensor image from boresight pixel.

Since the sun is a bright, symmetric object, a very simple method of estimating sun-angle is to find the peak reading from the sensor array and calculate the angle corresponding to that pixel. While this method achieves the two heuristic criteria identified above, intuitively it seems to ignore a lot of information (i.e. all the other pixels illuminated by sunlight). In most sensors the resulting accuracy is quite coarse. A sensor that resolves the sun-angle to better than one pixel is said to have *sub-pixel accuracy*. Another term for this property is *super-resolution.*

Improving a sensor's overall accuracy can be approached from two directions. The first involves enhancing the inherent resolution with a larger number of smaller pixels. If the overall sensor geometry remains the same, smaller pixels will produce better angular resolution. A significant drawback of this approach is that high resolution arrays are generally more expensive. A different approach is to improve the sensor's sun-localization ability through changes in the processing techniques.

1.3 Scope of Redesign

Improving sun-sensor performance requires the redesign of several aspects of the sensor system. Most changes will incur costs that can affect the commercial viability of the sensor. Direct component costs are important, however, changes that increase demand for volume, mass, power, or processing must also be carefully scrutinized. We can enumerate four categories of sensor design changes:

1. Algorithms: Improved routines can extract information more effectively from raw sensor data. With the help of intelligent processing strategies like super-resolution techniques, the angular accuracy of digital sun-sensors can be improved. Revised algorithms may not require any direct component changes, however, increased demand for processing power must be borne by the host spacecraft or through additional electronics.

2. Passive Components: Direct substitution of passive components (e.g. lenses, filters, and masks) may improve sensor accuracy, provided the replacements are of similar size and function to the original components. The costs of these changes are generally confined to the component that is replaced. Changing the detector illumination pattern by altering the sensor aperture is of particular interest.

3. Geometry: Modifications to volume and mass of sensor will affect the sensor performance characteristics. The cost impact of this type of change is generally proportional to the magnitude of the change requested. Care must be taken to avoid compramising other desirable properties such as the sensor field of view.

4. Active Components: The replacement of any electronic components such as the detector array can alter the native accuracy of the sensor. Direct costs and power requirements may increase substantially with these changes. Secondary effects such as radiation tolerance may also be affected. Some components can be very sensitive to noise.

In the balance between system performance and cost, the first two categories seem most promising. Although changing the geometry and other electronic components can provide substantial performance gains, these new designs cannot be implemented at minimal-cost. Therefore, the main focus of this study is to develop intelligent processing algorithms and changing the detector illumination pattern to improve the effective accuracy of digital sun-sensors.

1.4 Objectives

The main goal of this thesis is to analyze several approaches that can improve the angular accuracy of digital sun-sensors onboard a spacecraft through intelligent processing strategies and simple component changes. The main focus is on:

1. Using explicit knowledge of the illumination pattern in the processing algorithms. Some processing techniques derive greater advantage from *a priori* knowledge of the expected illumination pattern at the detector. The algorithms must be tolerant to random noise and interfering signals. Consequently, these algorithms will be able to permit precise localization of the Sun in the sensor image.
2. Making simple changes to the aperture geometry to provide an illumination pattern that can improve performance of the sensor. Changes to the detector illumination pattern can be implemented by altering the sensor's aperture mask. Since this is a superficial change, manufacturing costs will not increase.

A mathematical model of sun-sensor peformance is necessary to evaluate the impact of processing and mask pattern changes. A basic sensor model would allow tests as depicted in Fig 1.2.

The sensor model takes an input sun position, and with the help of sensor geometry description and noise, it generates an image. The algorithm under test interprets this simulated

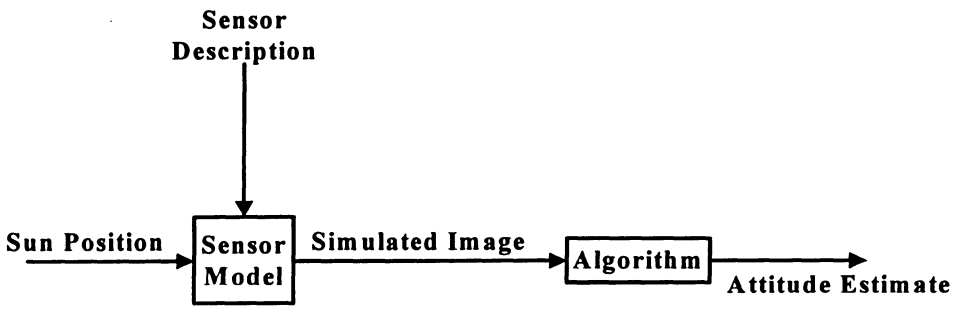

Figure 1.2 Testing procedure using a sun-sensor model.

image, producing an attitude estimate. Comparisons of the true and estimated postions then provide a measure of system performance.

Linking the sensor model and different processing techniques yields a system capable of estimating the displacement of sun illumination pattern. Using a baseline illumination pattern, the initial focus of this study is to examine whether intelligent processing techniques can increase system performance without drastically increasing the cost of the sensor system. The algorithm performance will be evaluated as a function of noise stength. The algorithms will also be tested with simple mask changes. The work will be further extended to evaluate different mask trends like, multiple slit patterns and changes to the native sensor resolution.

After comparing the performance of different illumination patterns, a methodical redesign of the sensor mask will be analyzed. The main objective is to determine an illumination pattern that resolves the sun-angle to better than one pixel. The final phase of this study will focus on developing a high fidelity noise model to demonstrate the effect of various noise sources on the performance of new processing techniques. The evaluation of the enhanced noise model will also include analyzing the effect of image artefacts on system performance.

1.5 Outline

The theoretical background of super-resolution algorithms and other methods of increasing the accuracy of sun-sensor is discussed in Chapter 2. A mathematical model of the digital sun-sensor is developed in Chapter 3. This includes the design of various super-resolution algorithms and also the development of a performance metric to evaluate the improvement in sun-angle estimation. Chapter 4 presents the performance of parametric and conventional super-resolution techniques on different illumination patterns. Simpel changes to detector illumination pattern against the performance of processing techniques will be evaluated to observe different mask trends. The detector mask optimization using Genetic Algorithms will be discussed in Chapter 5. High fidelity component noise models and the impact of image artefacts on system performance will be evaluated in Chapter 6. Finally, Chapter 7 includes conclusions and provides suggested directions for future research.

Chapter 2

BACKGROUND

Accurate orientation of a spacecraft or some of its onboard systems with respect to the Sun, the Earth, a star, or one of the planets is a challenging area in space technology. The Sun represents an excellent reference target and a sun-sensor is capable of high accuracy. The presence of the Sun cannot be ignored for eccentric orbits and space flight, and therefore, it is important to use it as an attitude reference. This chapter compares the advantages and drawbacks of different attitude sensors used in the ACS onboard a spacecraft, leading to an understanding of why sun-sensors were chosen as the major area of study in this thesis. In order to acheive greater accuracies, parametric algorithms could play a vital role in modern digital sun-sensors as image-processing techniques in estimating the sun-displacement. This chapter also provides the theoretical background and implementation of conventional and parametric algorithms used in this study.

2.1 Attitude Estimation

Attitude measurement is typically one of the major cost-drivers for the spacecraft bus. Multiple sensors are often employed because of the need to maintain 3-axis attitude information, depending on the requirements of different mission phases. This provides added accuracy and redundancy. Attitude sensor evolution is proceeding very rapidly, largely because of the availability of on-orbit processing. Microsatellites, nanosatellites, and picosatellites are making progress in moder space technology that holds major promise for

future explorations. Therefore, modern sensors should be smaller, lighter weight, and, at the same time more accurate.

2.1.1 Attitude Sensors

There are *two categories of attitude sensors*, and they are commonly used to complement each other in a measurement system [Fortescue, et al 2003]. The *reference sensor* (Sun-sensor, Star-sensor, Earth-sensor, Magnetometer, etc.) provides attitude data by measuring the direction of an object such as the Sun or a star, but during periods of eclipse they are unable to provide necessary information. *Inertial sensors* (Gyroscopes) measure continuously, but they measure changes in attitude, relative to a gyroscope rotor. They are useful for precise attitude sensing between inputs from reference sensors.

Magnetometers

Magnetometers are light weight, low power devices that measure both the direction and magnitude of the magnetic field. However, attitude measurements are not very accurate, since the magneitc field of the Earth is not precisely known. The limited accuracy can be attributed to the geomagnetic storms and magenetic fields in the satellite itself. The most common types of magnetometers are: Flux-Gate Magnetometers (FGM), Vector Helium Magnetometers (VHM), and Search Coil Magnetometers (SCM). FGMs are usually used for DC and very low frequency magnetic field measurements. They are used in all spacecraft either for orientation or for scientific purpose [Fortescue, et al 2003]. VHM instruments give better resolution and stability when compared to FGMs. However, FGMs are used widely due to lower mass, power, and relatively low cost. SCMs are mainly used to study the magnetic field variations in space plasma.

Magenetometers commonly suffer from two sources of error; one type resulting from slight sensor misalignements with respect to the coordinate axis, and the other from drifts in the quiescent point of the electronic components [Farrell et al, 1995]. These errors are typically seen in spinning spacecraft. Ongoing research in Imperial College[1] have shown that space borne magnetometers are designed to work over quite large magnetic field intensity ranges.

For Earth oribiting satellites, the magnetic field may approach thousands of nT, whereas in the solar wind the ambient field can be typically sub nT. To resolve such low fields, the magnetometer sensors are mounted on rigid booms away from the spacecraft to minmize magnetization effects from spacecraft materials and currents.

Earth Sensors

Earth-sensors are the primary means for determining the attitude of a spacecraft relative to the Earth. They are mainly used in communications, weather, and Earth resources satellites. Earth-sensors are also known as *horizon sensors* because they detect the transition between space and Earth, which occurs at the horizon. The common types of Earth sensors are: Earth albedo sensors, Horizon scanning sensors, and Horizon tracking sensors.

Earth albedo sensors rely on detecting sunlight reflected from Earth for thier operation. These sensors are not the most accurate because of the non-uniformity in the reflectance. This depends on the spacecraft-Earth-Sun angle (or phase angle). Changes to the phase angle vary the area of the illuminated Earth visible to the spacecraft. Horizon scanning sensors are generally used onboard a spacecraft to determine the nadir vector. Typically a scanning sensor sweeps across the Earth horizon to detect any abrupt change in infra-red signal between deep space and Earth. If the Sun does not interfere with the horizon crossings, then a single scan can provide an estimate of rotations, both roll and pitch, relative to the oribiting frame for the spacecraft [Wertz, 2001]. This type of sensor is useful over a wide range of spacecraft altitudes. They are operationally characterized by wide acquisition angles and fast response times [Coldrick, 1972]. Horizon tracking sensors are mostly used in geosynchronous orbits. They usually have one or more fixed fields-of-view that determine where the horizon lies along one sensitive axis. The angle between the line-of-sight of the tracker and a reference axis is measured and the roll and pitch attitude are computed.

1. Space and Atmospheric Physics, Imperial College, London, England - http://www3.imperial.ac.uk/spat/research/space_magnetometer_laboratory

The design of an earth-sensor and an evaluation of its capabilities and limitations require a knowledge of the spectral radiance emitted by the Earth. These sensors are usually coupled with sun-sensors to provide better accuracy.

Star Trackers

Stars provide the most accurate attitude reference for a spacecraft because they are point sources of light with a well-known angular position. Accuracies of 1 arc-second or better can be obtained [Fortescue, et al 2003]. Therefore, Star-sensors are used in most space systems that require high accuracy. With the introduction of low cost Chardged Coupled Devices (CCD) arrays and processors that are capable of providing efficient softwares, Star sensor technology is evolving very rapidly.

Typically, the attitude of a 3-axis stabilized spacecraft is determined by a Star tracker. The basic concept of the CCD Star tracker is very simple. Using a sensed image of the portion of the sky, stars can be located and identified by determining the transformation matrix (i.e. the attitude) which transforms the image to a known angular position of stars in the Star catalog. An estimate of the accuracy in locating stars is determined by the computing the star centroid. The implementation is however complex. Firstly, stars a point sources of light. Therefore, if the star images are smaller than the size of a pixel in the CCD array, the accuracy will be limited to the pixel size [Wertz, 2001]. The images are often defocused to spread them over a number of pixels and then the centroid of the star image can be computed accurately. Work done by [Liebe, 2002] proved that, an Active Pixel Sensor (APS) can help determine the centroid of a Star to approximately 1/10 of a pixel. The results coupled with low power consumption, simplified operation, and potentially better radiation robusteness, are the strengths of APS technology.

Gyroscopes

Gyroscopes use the conservation of angular momentum to sense and respond to changes in their orientation with respect to inertial space. One major disadvantage of this system is that it cannot sense the absolute attitude [Fortescue, et al 2003]. Consequently, a spacecraft using

star-sensors and gyros frequently use Earth-sensors and Sun-sensors for adequate operation during a fail-safe mode and attitude acquisition. Recent years have seen the development and introduction of gyroscopic sensors without moving mechanisms [Wertz, 2001]. Some common types of gyroscopes are: Ring Laser Gyroscope (RLG), Dynamically Tuned Gyro (DTG), Fibre Optic Gyroscope (FOG), and Hemispherical Resonator Gyroscope (HRG). Each of these gyros have the potential to improve the performance relative to the traditional ones.

2.1.2 Comparison

The performance and applications of typical attitude sensors are summarized in Table 2.1. The extent to which the ultimate accuracy is realized in given sensor depends upon its design, and this is related to its intended use. Each sensor has a typical FOV, and beyond this it does not provide any information.

TABLE 2.1 Typical Attitude Sensor Applications[a]

Sensor	Application	Accuracy	Cost
Magnetometer	Control momentum unloading using magnetic torquers	Low	Low
Sun-sensor	Attitude acquisition, yaw sensing	Medium	Low
Earth-sensor	Measure pitch and roll on earth oriented spacecraft	Medium	Medium
Star-sensor	Systems that require high accuracy	High	High
Gyroscopes	Used with Star-trackers to measure change in orientation	High	High

a. Adapted from [Wertz, 2001]

2.2 Super-Resolution Algorithms

Super-resolution is often used as a time delay estimation technique in radar and sonar processing. With minor alterations, algorithms designed for these applications can be used to estimate displacement rather than delay. Thus, temporal detection becomes a problem of spatial localization and the array illumination pattern replaces a time-series signal.

The processing techniques can be divided into two main classes:

1. Conventional Methods: These algorithms utilize little explicit information about what the signal or image should look like. They may include information about peak width and implicit assumptions about symmetry, however, it is rare that they include anything more than this. Some examples include, Peak Detection, and Centroiding.
2. Parametric Methods: These algorithms derive greater advantage from the *a priori* knowledge of the signal shape. Some examples are: MUSIC (MUltiple SIgnal Classification), ESPRIT (Estimation of Signal Parameters via Rotational Invariance Techniques), ML (Maximum Likelikood), Phase-correlation, etc.

Four algorithms are evaluated in this study out of which two of them are conventional algorithms common to spacecraft sensors while the other two are parametric algorithms employed in other fields of signal processing. This section provides some theoretical background of the different super-resolution algorithms used in sun-sensor processing. The implementation of peak-detection algorithm will be examined in Chapter 3

2.2.1 Centroiding Algorithms

In order to achieve improved performance in attitude estimation, the trend in measuring techniques have evolved from the use of analog centroiding devices towards digitized image data with a chosen centroiding algorithm. Star trackers utilize subpixel centroiding to increase the accuracy. In a survey paper by [Liebe, 2002], an algorithm for calculating centroids of a star image was examined. In the focussed image of a star, all photoelectrons from a star are

generated in a single pixel. But if the optics is defocussed, then the star will occupy several pixels which facilitates the use of centroiding method to achieve subpixel accuracy.

Consider a star image given by "image(x, y)". The image is shifted for pixels above a given threshold. A region of interest (ROI) window is aligned with the detected pixel in the centre. Then, the average pixel value on the border is calculated and subtracted from all pixels in the ROI window. The centroid (x_{cm}, y_{cm})[1] and DN (brightness) are then calculated from the subtracted pixels in the ROI.

$$DN = \sum_{x = ROIstart + 1}^{ROIend - 1} \sum_{y = ROIstart + 1}^{ROIend - 1} \text{image}(x, y) \tag{2.1}$$

$$x_{cm} = \sum_{x = ROIstart + 1}^{ROIend - 1} \sum_{y = ROIstart + 1}^{ROIend - 1} \frac{y \cdot \text{image}(x, y)}{DN} \tag{2.2}$$

$$y_{cm} = \sum_{x = ROIstart + 1}^{ROIend - 1} \sum_{y = ROIstart + 1}^{ROIend - 1} \frac{y \cdot \text{image}(x, y)}{DN} \tag{2.3}$$

The centroiding accuracy is proportional to the number of photons generated by the star.

Different centering techniques were investigated by [Stone, 1989] which includes, Gaussian functional fit, moment, median, and derivative search. The model chosen for a star image consists of a two-dimensional circular Gaussian with a flat sky background and smeared with Poisson noise. The adjustable parameters are:

- An image position described by $I(x_c, y_c)$ within the scan box.
- The rectangular scan box dimensions given by (n_x, n_y).
- The aperture size a in arc-seconds.

1. Equations taken from [Liebe, 2002].

Symmetric Gaussian

The Gaussian method consists of fitting a symmetric Gaussian function with a flat sky background to each of the coordinate marginal distributions. An array of count data $I(x, y)$ can be reduced to a one-dimensional distribution by forming marginal distributions in each coordinate directions. Marginal distribution in the x coordinate can be defined as [Stone, 1989]:

$$M(x) = \sum_{y} I(x, y) \tag{2.4}$$

A similar expression for y can be developed. The basic equation for the Gaussian function is given by,

$$M(x) = B + H\exp\left[-\frac{(x - x_c)^2}{2R^2}\right] \tag{2.5}$$

where B is the background level defined by $B = n_y b$ (n_y is the array cross dimension, and b is the sky-background level expressed in units of counts arcsec^{-2}). H is the central image height in the marginal distribution which is expressed in terms of total number of counts N, and R is the rms half width of the image.

$$H = \frac{N}{(2\pi)^{1/2} R} \tag{2.6}$$

This algorithm requires a solution for the four parameters expressed in (2.5), which can be easily linearized with a first-order Taylor's expansion and solved by iterative least squares.

Moment

In this method, the image centroid is set equal to the first moment of the marginal distribution. The mean of outer marginal endpoints can be used to calculate the background level B. The basic equation is given by,

$$x_c = \frac{\sum_x x[M(x) - B]}{\sum_x [M(x) - B]} \tag{2.7}$$

The moment algorithm, as defined above, was investigated by [Auer & van Altena, 1978], and found to be less accurate than the functional fit to a symmetric Gaussian. This method was found to be sensitive to count levels in the background and performed badly for centred star images. Since the points located far away from the image centre are weighted in the solution by the square of their distance from it, the centering process underwent serious degradation.

Median

In this technique, the centre of an image x_c is defined to be a value of x that divides the starcount data into two equal halves. After the background level is subtracted from each element of the marginal distribution, a cumulative distribution of counts $Q(x)$ is formed and the median is defined as the value of x for which,

$$Q(x) = \frac{1}{2} Q(x_{max}) \tag{2.8}$$

Interpolation was used to define the value of the median since this distribution function was defined empirically. This centering method is not sensitive to wild points in the marginal data and performed better with faint star images [Chui, 1977]. A weakness of this method was that the interpolation was found to be sensitive to the size of the pixel spacing and the amount of noise associated with the count data in the central part of the image.

Derivative Search

For the derivative search method, once the marginal is formed, a smooth derivative $G(x)$ is determined at each marginal grid points by,

$$G(x) = \frac{1}{2}[M(x+1) - M(x-1)] + \frac{1}{4}[M(x+2) - M(x-2)] \tag{2.9}$$

This array is searched for its minimum and maximum values and a line is fit by the least squares to the points in these two limits. Since this method only uses the central part of the image, it was found to be less accurate than the gaussian method [Chui et al, 1979]. This method cannot be used for centering saturated images. The greater speed of this technique allows it to be used for the preprossesing of large amounts of image data.

The following important observations were made by [Stone, 1989] when all the above mentioned methods were tested:

- The derivative search technique is significantly less accurate than other methods and performs worse when considering high sky-background levels. This method is very sensitive to noise in the central part of the image.
- The moment method is an inferior centering technique when compared to other centering algorithms with increasing sky-background levels.
- For high S/N images or low sky-background levels, gausian and median methods display similar accuracy. The Gaussian method is the standard method used in image processing applications for astrometry, and the observations made by [Stone, 1989] suggested that it was not necessarily the best method for all conditions. For centering weak stellar images subjected to high sky-background levels, the Gaussian method can be very slow.
- For increased sky levels, median routine is less accurate. Increased sky-count levels add noise to the marginal distributions which inturn degrades the centering process.

A modified moment method, when compared to the traditional moment method, can be less sensitive to noise in the sky-background level. In this method, most of the counts in the background are eliminated by defining a threshhold. Therefore, by only considering count levels above the threshold in the centering process, the inaccuracies introduced by noise can be eliminated. This offers a very significant improvement over that of the traditional moment method.

Centroid calculation is a common super-resolution technique in spacecraft sensor processing. This processing technique is currently used in most of the digital and analog sun-sensors. The centroiding method used in this study is similar to that of the modified moment method. Assuming that the illumination on the detector is symmetric about the displacement τ, and that light from the sun falls on several pixels in the array, the centroid calculation improves the estimate of the peak location. The centroid is calculated over a user-defined window surrounding the peak value (Fig 2.1).

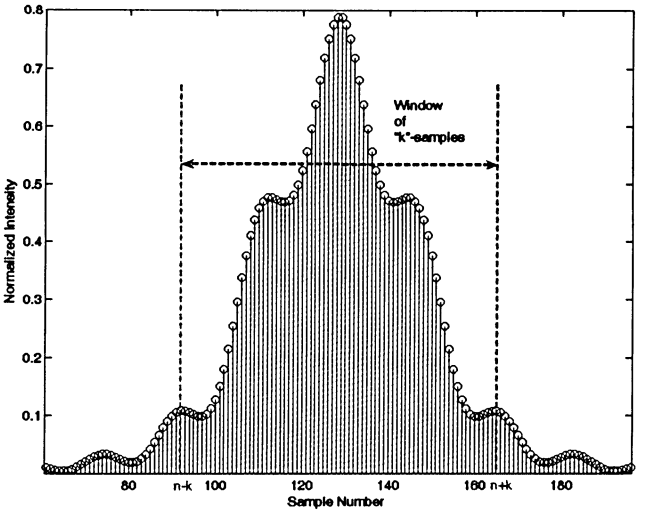

Figure 2.1 Windowing of peak image for centroid calculation

To estimate the displacement of $I[n]$, the index of the brightest pixel is first found using a simple peak-detection algorithm. The centroid is then calculated from the neighbouring pixels:

$$\tilde{\tau} = \frac{\sum_{l=n_{peak}-k}^{n_{peak}+k} (l\Delta X)\cdot I[l]}{\sum_{l=n_{peak}-k}^{n_{peak}+k} I[l]} \tag{2.10}$$

The centroiding algorithm can also be modified to estimate the displacement of multiple peak illumination patterns. As a first measure, the centre of the pattern is found using the peak-detection algorithm. One of the N_P peaks is expected to be found at each of the locations given by:

$$n_i = n_{peak} + d_i \tag{2.11}$$

The centroid of each peak $\tilde{\tau}_i$ is then calculated individually from ((2.10)). Finally the results are averaged to yield a displacement estimate for the entire pattern:

$$\tilde{\tau} = \sum_{i=1}^{N_p} (\tilde{\tau}_i - d_i \Delta X) \tag{2.12}$$

For any particular illumination pattern, some hand tuning is necessary to select an appropriate window size. If the hand tuning is not done properly, it can bias the estimate of $\tilde{\tau}$. The implementaion of this algorithm for sun-sensor processing and proper selection of the centroid window size will be examined in Chapter 3.

2.2.2 Phase Based Algorithms

Phase Correlation Method

The ability to detect and estimate lateral shifts between similar images is an integral part of many image processing applications. The phase-correlation method is a popular choice [Foroosh & Zerubia, 2002] due to its robust performance and computational simplicity. The phase-correlation method is based on the Fourier shift property. Specifically, a shift in the coordinate frame of two functions results in a linear phase differences in the Fourier transform of the two functions.

Phase correlation method can be applied to both two-dimensional and one-dimensional images. For a two-dimensional case, this method can be described as follows:

Let $f_1(x, y)$ and $f_2(x, y)$ be two functions that are given by,

$$f_2(x,y) = f_1(x-x_0, y-y_0) \tag{2.13}$$

According to the Fourier shift property,

$$\hat{f}_2(u,v) = \hat{f}_1(u,v)\exp(-j(ux_0 + vy_0)) \tag{2.14}$$

Hence the normalized cross power spectrum is given by

$$\frac{\hat{f}_2(u,v)\hat{f}_1(u,v)^*}{\left|\hat{f}_2(u,v)\hat{f}_1(u,v)^*\right|} = \exp(-j(ux_0 + vy_0)) \tag{2.15}$$

where * indicates the complex conjugate, (u, v) are the Fourier domain coordinates, and x_0 and y_0 are the magitude of the horizontal and vertical shifts that occur between f_1 and f_2. One way to solve (2.15) for (x_0, y_0) is to first inverse Fourier transform the normalized cross power spectrum. The result would be $\delta(x-x_0, y-y_0)$ which is a Dirac delta function centred at (x_0, y_0). Replacing the Fourier transform by the Discrete Fourier Transform (DFT) and the Dirac delta function by a unit impulse, these results still hold and work remarkably well.

PCM is very robust to types of noise that are correlated to the image function, e.g., uniform variations of illumintation, offsets in average intensity, and fixed gain errors due to calibration. This property also makes PCM suitable for sub-pixel registration across different spectral bands [Foroosh & Zerubia, 2002]. Some of the noise sources mentioned above can be found in sun-sensor images as well.

Linear-phase Algorithm

In this study, however, a different method was developed to improve the accuracy of sun-sensor image processing. The method is called *Linear-phase Algorithm*. This method is quite similar to PCM, but will be applied to one-dimensional sun-sensor illumination patterns. The linear-phase algorithm is also based on the fundamental principles of DFT.

Since a signal sampled in space can be substituted for the conventional time-sampled signal, the time delay in Digital Signal Processing (DSP) can be considered to be analogous to the

displacement τ of the signal received by the sun sensor. The linear-phase algorithm is an efficient method for estimating the effective resolution of the sensor.

Consider a discrete signal and its *Discrete Fourier Transform* (DFT):

$$I[n] \overset{DFT}{\leftrightarrow} S[k] \tag{2.16}$$

A linear shift in the discrete signal can be represented using the properties of DFT as shown below:

$$I[n-\alpha] \overset{DFT}{\leftrightarrow} S[k]e^{-j\frac{2\pi k\alpha}{N}} \tag{2.17}$$

In the second case, the illumination pattern has been shifted by α samples. Therefore, a shift in the space domain is equivalent to a multiplication by a linear-phase term in the frequency domain. It is significant to notes that this interpretation holds good even if α is not an integer.

Defining $S_0[n]$ as DFT of the zero shift signal and $S_\alpha[n]$ as the DFT of the shifted version, the exponential term can be isolated as follows:

$$Y[k] = \frac{S_\alpha[n]}{S_0[n]} = e^{-j\frac{2\pi k\alpha}{N}} \tag{2.18}$$

If ψ is the phase angle of $Y[k]$, then it can be shown that:

$$\psi[k] = -\frac{2\pi k\alpha}{N} \tag{2.19}$$

The estimate of τ can be obtained from the calculated slope and the sample number n as follows: First, perform a least-squares fit using a sub-set of $\psi[k]$ to get an estimate $\tilde{\alpha}$ of the slope. An estimate of the displacement $\tilde{\tau}$ can then be calculated using:

$$\tilde{\tau} = \tilde{\alpha} \cdot \Delta X \tag{2.20}$$

2.2.3 Eigenanalysis

A popular group of parametric *time-delay estimation* (TDE) techniques exploit the eigen-structure of the system covariance matrix to achieve super-resolution estimates. These techniques divide the cross-correlation matrix of the array signals into signal and noise subspaces using eigen-value decomposition (EVD). Originally formulated for direction-of-arrival (e.g. MUSIC [Schmidt, 1986]) and spectral (e.g. RELAX [Li & Stoica, 1996]) estimation, these techniques have also been used to estimate signal time delays. One of the main advantage of these techniques is their tolerance of random noise and interfering signals. Other applications of eigenanalysis techniques include sonar, radar, radio-astronomy, seismology, and array processing. The illumination displacement problem encountered in sun-sensor processing is analogous to the time-of-arrival (or time-delay-of-arrival) problems in radar/sonar processing. The scope of this study does not allow an exhaustive comparison of the various extant eigenanalysis techniques. Instead, the selection of the algorithm is purely based on how well these algorithms can perform.

This particular algorithm is based on the *Eigenanalysis and Sequential Quadratic Programming (ESQP)* technique proposed by [Ge et al, 2004]. Since the sun-displacment estimation problem is simpler than that addressed by the ESQP algorithm, only the eigenanlysis and not the Sequential Quadratic Programming parts of the algorithm is necessary in this study. The main advantage of this algorithm is that it does not demand the presence of a large number of samples for the estimation of linear shift in the signal.

Following [Ge et al, 2004] with some modifications to nomenclature, the continuous reference signal and the delayed signal are modeled as:

$$\begin{aligned} r_1(X) &= a_1 \cdot s(X) \\ r_2(X) &= a_2 \cdot S(X-\tau) + w(X) \end{aligned} \tag{2.21}$$

where $r_1(X)$ is the ideal signal and $r_2(X)$ is the delayed signal, a_1 and a_1 are the corresponding signal amplitudes, τ is the unknown delay of the received signal, and $w(X)$ is the AWGN process. When these signals are sampled at a sampling spacing ΔX, they can be written as

$$\begin{aligned} r_1[n] &= a_1 \cdot s(n\Delta X) \\ r_2[n] &= a_2 \cdot s(n\Delta X - \tau) + w(n\Delta X) \end{aligned} \qquad n = 0, 1, \ldots, N-1 \tag{2.22}$$

where N is the length of the sequences.

Zero-padding $r_1[n]$ and $r_2[n]$ to length $K_x = 2N-1$, the cross-correlation function between $r_1[n]$ and $r_2[n]$ can be evaluated using circular correlation as

$$\begin{aligned} R_{r12}[\tau] &= \sum_{k=0}^{K_x-1} r_1(n-\tau) \cdot r_2^*(n) \\ &= \sum_{k=0}^{K_x-1} \left(a_1 a_2^* |S[k]|^2 e^{j\frac{2\pi}{K_x}k\tau} + a_1 S[k] W^* k \right) e^{-\frac{2\pi}{K_x}k\tau} \end{aligned} \tag{2.23}$$

where $S[k]$ and $W[k]$ are the discrete Fourier transforms of $s[n]$ and $w[n]$ respectively. The cross-correlation function helps reject the effects of noise. This ensures good time-delay resolution [Knapp & Carter, 1976].

To estimate τ for any particular trial, the cross-correlation series $R_{r12}[k]$ is further zero padded to length $2K_x-2$, and the correlation function $R_x[l]$ is found based on (2.23) according to *Wiener-Khinchine* theorem:

$$R_x[l] = DFT^{-1}[|R_{r12}[k]|^2], \qquad (k, l = 0, 1, \ldots, 2K_x-2) \tag{2.24}$$

The truncated covariance matrix $\hat{R}_{sub\_x}$ is then,

$$\hat{R}_{sub\_x} = \begin{bmatrix} R_x[0] & R_x^*[1] & \ldots & R_x^*[N-1] \\ R_x[1] & R_x[0] & \ldots & R_x^*[N-2] \\ \vdots & \vdots & \ddots & \vdots \\ R_x[N-1] & R_x[N-2] & \ldots & R_x[0] \end{bmatrix} \tag{2.25}$$

Solving for the eigenvectors of the covariance matrix in (2.25), the noise subspace matrix $\hat{E}_{sub,n}$ can be evaluated corresponding to $\hat{R}_{sub\_x}$ from the noise eigenvectors.

The vector function $b(\tau)$ can then be formed from the squared magnitude of S and a complex exponential term:

$$b(\tau) = \left[|S[0]|^2 \;\; |S[1]|^2 e^{j\frac{2\pi}{K_x}\tau} \;\; \ldots \;\; |S[K_x - 1]|^2 e^{j\frac{2\pi}{K_x}(K_x-1)\tau} \right]^T \tag{2.26}$$

This expression represents a model of the useful component of received signal; it should have little projection onto the noise sub-space. Note the similarity to (2.17). Therefore, this can be truncated to length N to form the sub-vector $b_{sub}(\tau)$. This noise subspace is then used along with the known properties of the ideal zero-delay signal to estimate τ based on the following criterion

$$\hat{\tau} = \arg\min_{\tau} \left\{ \left\| b_{sub}^H(\tau) \hat{E}_{sub,n} \right\|^2 \right\} \tag{2.27}$$

Any suitable algorithm can be used to solve this minimization problem and estimate the illumination displacement.

2.3 Summary

Detailed analysis of various centroiding algorithms used in Star sensors were investigated. It was established that certain centering algorithms when slightly modified to suppress the sky background below a prechosen threshold level can significantly improve the accuracy of star image processing. The theoretical background of centroiding algorithm was also introduced. Parametric algorithms play a vital role in estimation of lateral shift in two similar images. The linear-phase algorithm was introduced in this section. It was found to be similar to the Phase correlation method used widely in image processing for subpixel registration. Another parametric algorithm was also examined, eigenanalysis. Therefore, the four algorithms that will be used in this study are: Peak-detection, Centroiding, Linear-phase, and Eigenanalysis.

Chapter 3

DESIGN EVALUATION FRAMEWORK

A mathematical model of sun-sensor performance is necessary to evaluate the impact of processing and mask pattern changes. As a starting point, a commercially available sensor made by Sinclair Interplanetary is chosen to provide the baseline parameters for the sensor model used in this study. Since the initial objective of this study is to demonstrate a proof-of-concept that evaluates the performance of super-resolution algorithms, rather than a complete solution to the sensor redesign question, the model need not replicate the hardware performance precisely. The derived sensor model will provide a qualitatively similar output by using the geometric parameters of the real sensor. This observation permits a series of simplifying assumptions.

3.1 The Sinclair Interplanetary SS-256 Digital Sun-Sensor

The Sinclair Interplanetary SS-256 is a modern digital sun-sensor. This device measures the angular position of the sun within a 70° half-angle field-of-view. It cosists of an aperture mask, also known as an *Optical Mask*, which is made from a disc of mirrored glass with fine slits cut into it using a high-power laser. Behind the mask is a *natural density filter*, and a detector array. When the sunlight hits the sun-sensor, the opaque portions of the aperture mask blocks the incoming light. The sunlight which passes through each of the slits intersects the linear array creating a series of bright spots. The task of the processing algorithms is to

detect and identify the bright peaks in the sensor image to help determine the position of the Sun.

Each slit is of width, $w = 0.025mm$. The natural density filter has a moderate index of refraction $n_{glass} = 1.51$. The filter thickness, z_s, is $2.37mm$. The detector is a single $16mm$-long linear array of 256 pixels. As mention earlier, SS-256 will be used to provide baseline sensor geometry. SS-256 is a two-axis sensor. The model developed for this study will only have slits along one-axis. Therefore, here is a description of what a one-dimensional version would look like:

The general character of the optical propagation from the mask to the detector can be obtained by calculating the Fresnel Number N_F of one of the slits:

$$N_F = \frac{w^2}{\lambda z_s} \tag{3.1}$$

Taking into account the index of refraction, the Fresnel Number for any particular free-space wavelength λ_0 is then:

$$N_F = \frac{w^2 n_{glass}}{\lambda z_s} \tag{3.2}$$

The detector sensitivity peaks at $\lambda_0 = 700nm$. At this wavelength $N_F = 0.14$. This value indicates that the optical characteristics near the sensor boresight lie between the Fresnel and Fraunhofer regimes.

The non-dimensional distance X, can be calculated from the actual distance x [Goodman, 1996]:

$$X = \frac{x}{\sqrt{\lambda z_s}} \tag{3.3}$$

Thus, the limits of the SS-256 pixel array can be calculated giving, $|X_{max}| \cong 250$. Based on these values the illumination pattern for the sensor model will be derived.

3.2 Model Design

A general test scheme was presented in Chapter 1. An ideal sensor model would allow tests of the sort depicted in Fig 3.1. The model takes an input sun angle θ and along with the sensor mask and geometry it generates a discrete intensity map $I(n)$, indexed by pixel number n. The algorithm under test interprets this image producing an estimate of the sun angle $\tilde{\theta}$. Comparisons of the true and estimated angles then provide a measure of system performance.

Exact replication of the SS-256 behaviour was unnecessarily complex for the proof-of-concept nature of this study. Using the characteristic parameters from the SS-256 sensor

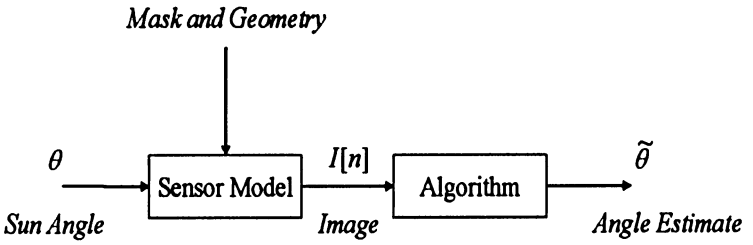

Figure 3.1 Testing using an ideal sensor model

derived above, a simple and computationally tractable model was developed to evaluate algorithm performance. These assumptions are consistent with the simple device shown earlier in Fig 3.1.

To simplify the model and the array illumination calculations, the aperture patterns considered in this study will consits of slits in one-axis only. This change makes the modelling and estimation tasks easier but the modelled device is still physically realizable. Subsequent assumptions further simplify the image synthesis. These changes involve more substantial compromises in the model's quantitative accuracy but the resulting images are still qualitatively similar to those generated by the real sensor.

- Monochromatic Illumination. Light propagating through the sensor is considered to consist of a single wavelength. The wavelength chosen

corresponds to the peak sensitivity of the imaging array (this could be physically approximated by substituting a band-pass filter for the natural-density filter).

- Plane-Wave Illumination. Although the Sun is an extended source, treating the incoming light as uniform plane waves makes propagation calculations substantially easier. Although this change makes the model less accurate, it does not necessarily make the estimation process easier.
- Linear displacement replaces angular rotation. Instead of specifying an incidence angle explicitly, the sun position is characterized by shifting the array illumination pattern through a linear displacement τ. Performance is characterized by the ability to resolve small displacements, rather than small angles. From Fig 1.1, θ is the angle between (z-x) projected sun vector and the z-axis. The incidence angle can be estimated from the displacement τ by, $\theta = \text{atan}\left\{\frac{\tau}{z_s}\right\}$. This does not restrict the Sun to one-dimension. Only the measurement will be restricted to one-dimension.
- Pixel detectors approximated by sampling of illumination pattern. Each pixel in a physical sensor counts photons incident on a finite collection area. The inaccuracy in modelling due to a sampling rather than intergrating the array illumination is a function of the spatial-frequency content of the illumination pattern. Provided spatial aliasing is not significant, the errors will be minor.

As a result of these assumptions the testing process slightly deviates from the procedure discussed above. A revised diagram of the process is shown in Fig 3.2.

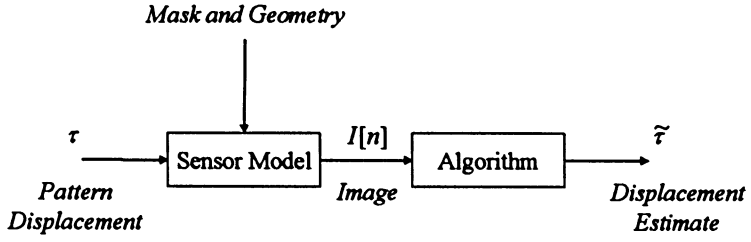

Figure 3.2 Testing using the simplified sensor model

3.3 Analytical Sensor Model

As discussed in Section 3.2, the simplified sensor model must take the specified displacement τ and calculate the resulting discrete image $I[n]$. Treating the aperture as an infinite narrow slit, [Goodman, 1996] treatment of a square aperture to derive the exact Fresnel solution to diffraction through the slit is adapted. Using the non-dimensional distance, X, presented in ((3.3)) and the Fresnel Number N_F of the slit from ((3.1)), the continuous intensity pattern at the image plane is given by:

$$I_c(X) = \frac{1}{2}\{[C(\alpha_2) - C(\alpha_1)]^2 + [S(\alpha_2) - S(\alpha_1)]^2\} \tag{3.4}$$

where $C(\alpha)$ and $S(\alpha)$ are the Fresnel Cosine and Sine integrals:

$$\begin{aligned} \alpha_1 &= -\sqrt{2}(\sqrt{N_F} + X) \\ \alpha_2 &= \sqrt{2}(\sqrt{N_F} - X) \end{aligned} \tag{3.5}$$

The pixel spacing ΔX in the N-pixel array is given by:

$$\Delta X = \frac{2X_{max}}{N} \tag{3.6}$$

since the array extends from $-X_{max}$ to X_{max}. Shifting the illumination pattern by τ, sampling the illumination pattern and adding noise gives:

$$I[n] = I_c(n\Delta X - \tau) + w[n] \tag{3.7}$$

where $w[n]$ represents a sensor noise process with mean μ, and variance σ_n^2.

Although several noise sources are typically considered when using pixel sensors [Healey & Kondepudy, 1994], the sensor model used to evaluate the performance of different super-resolution algorithms includes only an Additive White Gaussian noise (*AWGN*) term with zero mean, and variance σ_n^2. A realistic noise model will be discussed in Chapter 6.

In laboratory testing, the observed image-to-image standard deviation with the SS-256 sensor was approximately 0.3% of the peak intensity. Since this characteristic level is quite low, the inaccuracy introduced by using a single AWGN noise term rather than component noise models, was judged to be negligible. Tests performed at high noise levels (Chapter 4) are less representative of true sensor images but could represent generic image degradation.

Some refinement of sensor parameters (N_F and X_{max}) was required to produce images matching those of the SS-256 sensor (Fig 3.3.(a)). Reducing X_{max} to 50, widens the simulated illumination pattern and this modification compensates for the extended size of the sun (Fig 3.3.(b)). Increasing N_F to 1.0 improved the representation of peak shape (Fig 3.3.(c)).

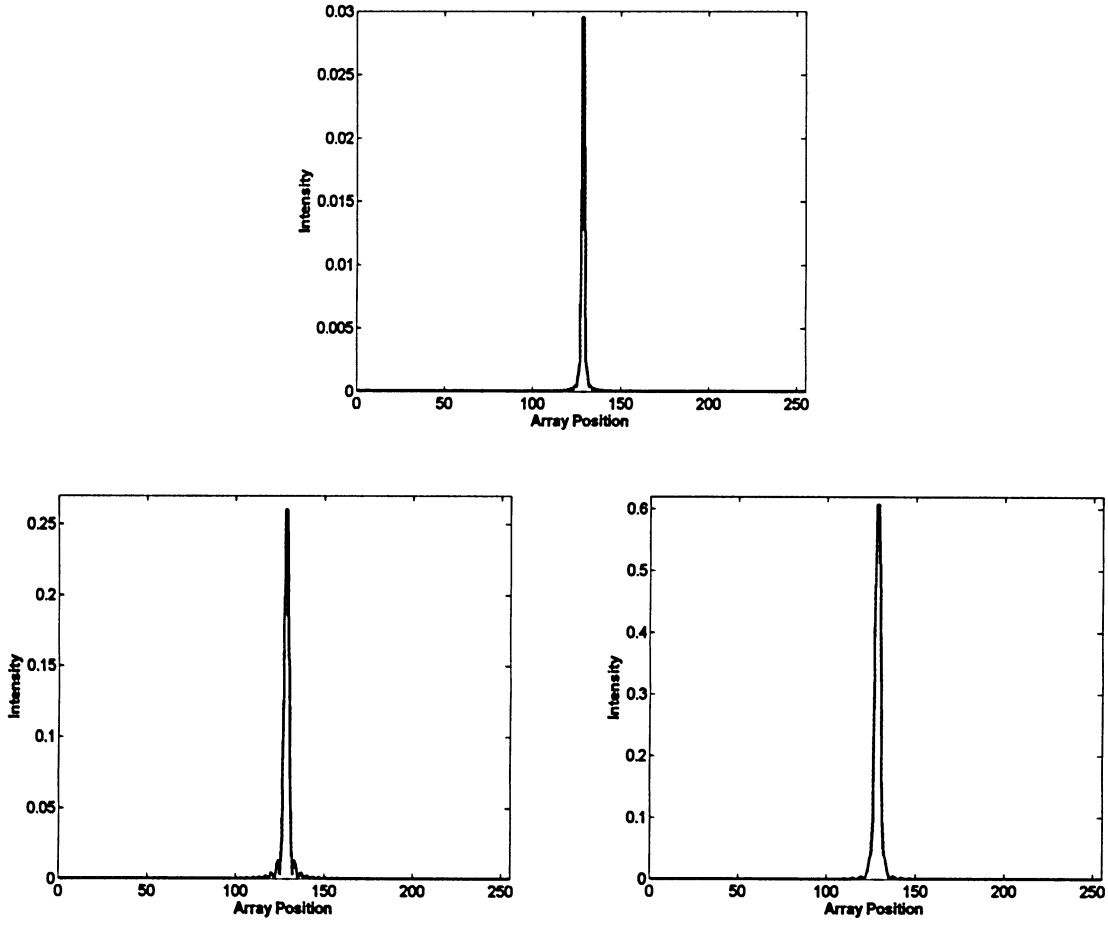

Figure 3.3 Variations in illimination patterns. (a.) SS 256 sensor paramters (N_F and X_{max}), (b.) Reducing to 50, and (c.) Increasing N_F to 1.

A pattern with N_P peaks can be described by a vector,

$$D = \{d_1, d_2, \ldots, d_{N_p}\} \tag{3.8}$$

which specifies the offset, in pixels, from the centre of the pattern to each peak. For evaluating the performance of multiple peak illumination patterns, the narrow one-peak pattern is retained and different illumination patterns are produced by altering the number of peaks. Multiple peak patterns are formed by superimposing shifted single-peak patterns. Provided the peaks are not so close that they correspond to overlapping slits in the aperture, this superposition is valid. This study mainly considers only two types of patterns: narrow peak patterns, and wide peak patterns.

TABLE 3.1 Baseline Parameters of Illumination Patterns

Reference	X_{max}	N_F
Narrow peak pattern	50	1
Wide peak pattern	25	1

A sensor model used to evaluate the effect of one-peak illumination pattern is shown in Fig 3.4. The narrow peak pattern was developed using $X_{max} = 50$ and the wide peak pattern was synthesized using $X_{max} = 25$. A second sensor model was derived to evaluate the effect of the number of peaks in the illumination pattern on sensor performance. A sample pattern with the narrow and wide two peak cases is shown in Fig 3.5.

TABLE 3.2 Identifier for Illumination Patterns

Identifier	Reference
N1	Narrow, one-peak pattern
W1	Wide, one-peak pattern
N2	Narrow, two-peak pattern
W2	Wide, two-peak pattern

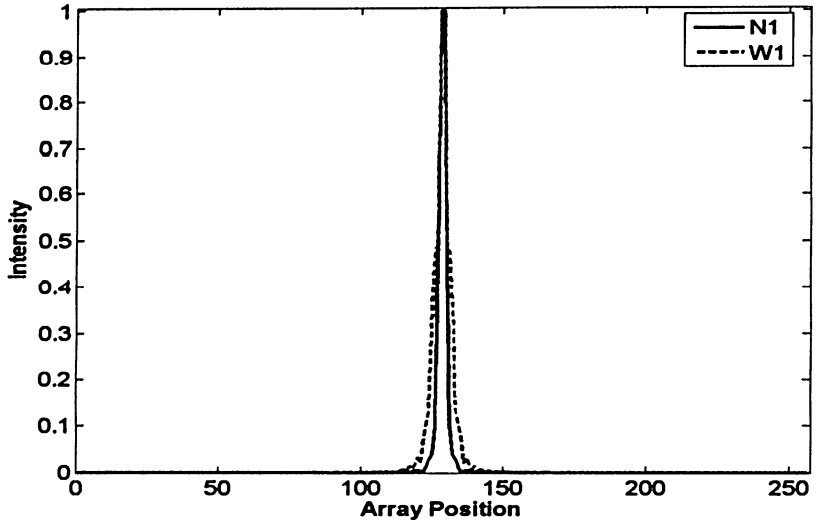

Figure 3.4 One peak illumination pattern (no noise), showing narrow (N1) and wide (W1) peaks.

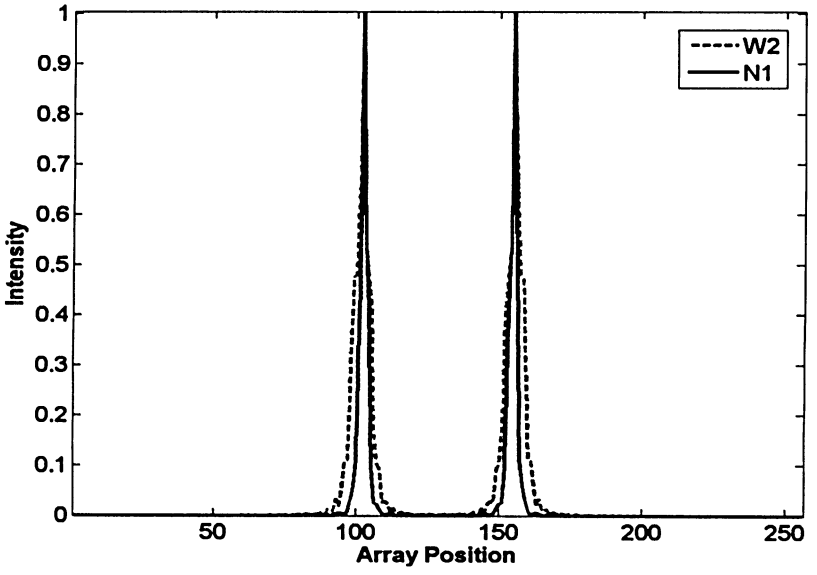

Figure 3.5 Two peak illuminaton patterns (no noise), showing narrow (N2) and wide (W2) peaks.

The peak spacing is somewhat arbitrary, however, the selection was guided by the principle that an illumination pattern similar to the SS-256 was desirable.

3.4 Implementing Super-Resolution Techniques

The theoretical framework of the Centroiding, Linear-phase, and Eigenalaysis algorithms were discussed in Chapter 2. This section provides a detailed description of how each of these algorithms are implemented for sun-sensor processing. Some of the algorithms require manual and automatic tuning to deal with multiple peak patterns. The theory behind peak-detection algorithm will also be examined.

3.4.1 Peak Detection

Peak-detection is a baseline conventional algorithm. This algorithm is computationally trivial; it simply searches the sensor image for the brightest pixel and calculates sun position from the location of that pixel:

$$n_{peak} = \arg\max_{n}(I[n]) \qquad n = -\frac{N}{2}\ldots\frac{N}{2}$$
$$\tilde{\tau} = n_{peak}\Delta X \tag{3.9}$$

For single-peak patterns the implementation of this algorithm is very simple. In the case of multiple peak patterns, this algorithm can be modified to search for a set of bright pixels with a specified spacing. A pattern with N_P peaks can be described by a vector given in (3.8), which specifies the offset, in pixels, from the centre of the pattern to each peak.

The pattern in the image can then be located in a max-min fashion:

$$n_{peak} = \arg\max_{n}(\arg\min_{i}(I[n+d_i])) \tag{3.10}$$

This algorithm is not very sophisticated, however, it can be useful as a comparison for other methods of delay estimation.

3.4.2 Centroiding

For any particular illumination pattern, some hand tuning is necessary to select an appropriate window size. The effect of not selecting an accurate window size can lead to discrepancies in the final results.Fig 3.6 explains this effect in detail.

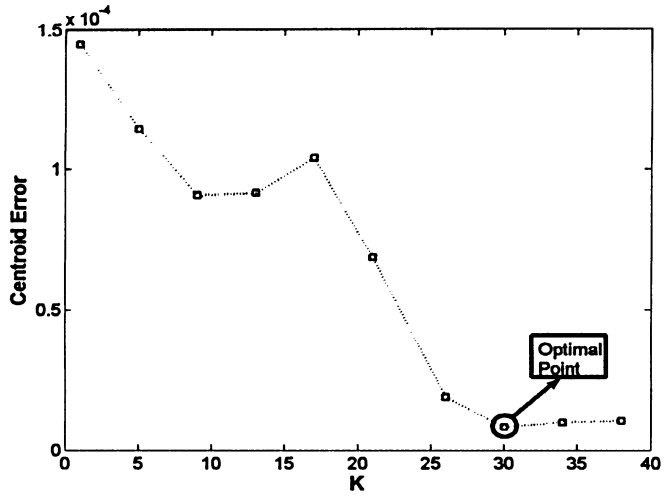

Figure 3.6 Inaccuracies in selecting the appropriate centroid window size.

Values in the x-axis represents the number of samples in one particular centroid window, k. It is clearly visible from Fig 3.6 that, there is an optimal centroid window which gives the minimum centroid error. The super-resolution performance of this algorithm is highly sensitive to the choice of window width k. If the window chosen is too wide, the extra points simply add noise. Conversely, if the window chosen is too narrow, we may capture the peak asymmetrically. This introduces a bias in the estimate of τ. Therefore, in the presence of increased noise amplitude, the position of the peaks will be distorted and these noise spikes can influence the algebraic computation of the centroid. This algorithm requires some hand-tuning to find the best window size for any given illumination pattern. In practice, this is usually a minor drawback. In a low-noise environment, centroiding is an effective and computationally efficient method of estimating the displacement in the signal received by the sun sensor.

3.4.3 Linear-Phase

In Section 2.2.2 it was shown that, an estimate of τ can be obtained from the phase angle $\psi[k] = -\frac{2\pi k\alpha}{N}$ by,

1. Perform a least-squares fit using a sub-set of $\psi[k]$, to get an estimate of α of the slope
2. Estimate of the displacement τ can then be calculated using

$$\tilde{\tau} = \hat{\alpha} \cdot \Delta X \tag{3.11}$$

Fig 3.7 shows a plot of $\psi[k]$, for a zero noise illumination pattern, and for a pattern degraded with 1.5% noise.

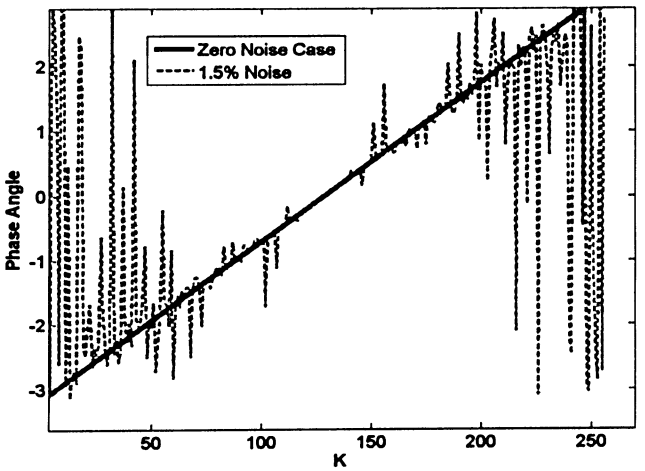

Figure 3.7 Phase angle for a zero noise pattern, and a noisy pattern.

Zeros in the spectrum of $I_0[n]$ cause severe distortions in the phase function. In Fig 3.7, for the illumination pattern degraded with 1.5% noise, distortions in the phase function can be seen in the areas of higher frequency (extreme right and left regions). The zero-noise illumination pattern represents the case of ideal $\psi[k]$. Therefore, this distortions must be avioded while estimating the slope of $\psi[k]$. To maintain good performance, the least-squares fit must be performed using a sub-set of $\psi[k]$. This selection process requires a combination

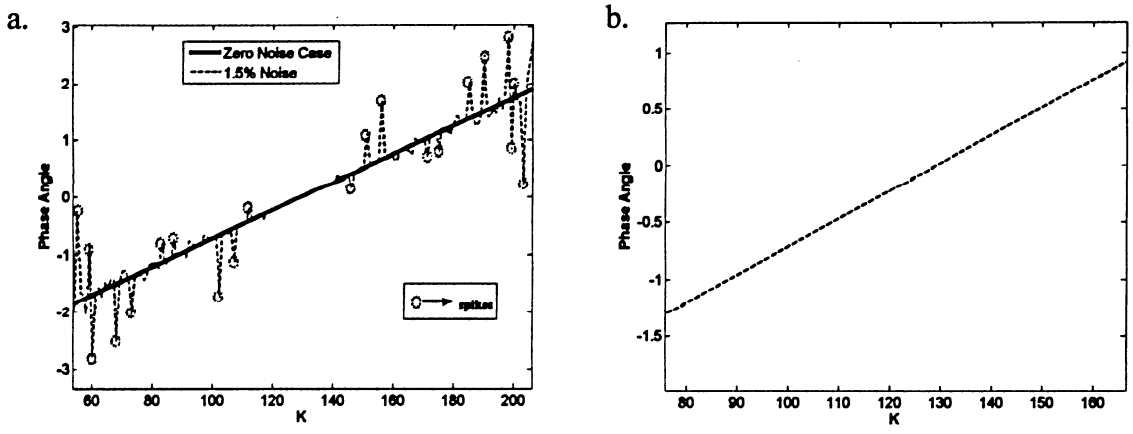

Figure 3.8 Restricting the calculations to a linear-region (a.), and thresholding the spikes (b.).

of manual and automatic tuning. For a given illumination pattern, the user must first identify the region of 'relatively' linear phase near zero frequency as shown in Fig 3.8.(a). Some distortions would still exist. Therefore, automatic thresholding can further eliminate these localized distortions (Fig 3.8.(b)). The calculations can then be restricted to the linear region of $\psi[k]$. No further modifications to the algorithm are needed to deal with multiple-peak patterns.

3.4.4 Eigenanaylsis

No modifications or tuning of this algorithm was necessary between trials or with different illumination patterns. The eigenanalysis algorithm can be summarised as follows:

1. Compute the cross-correlation function between $r_1[n]$ and $r_2[n]$ by using circular correlation.
2. Zero pad the squared envelope of the cross-correlation series $R_{r12}[k]$, and compute the IDFT of $|R_{r12}[k]|^2$. Then form the estimate of the covariance matrix $\hat{R}_{sub\_x}$.
3. Compute the noise subspace matrix $\hat{E}_{sub\_n}$ from the noise eigenvectors.
4. Using a simple minimization routine in MATLAB to solve for $\tilde{\tau} = \arg min\{\|b_{sub}^H(\tau)\hat{E}_{sub\_n}\|\}$, and estimate $\tilde{\tau}$.

3.5 Performance Metric

Linking the analytical sun-sensor model and one of the processing algorithms, yields a system capable of estimating the displacement of sun illumination pattern. In order to quantitatively assess the results of these simulations, a suitable performance metric is required. To rate each algorithm's performance, a quantity called the *effective resolution* is derived.

In order to evaluate an algorithm's performance, the true displacement τ is treated as a random variable. Since these algorithms are memoryless, each displacement estimate is based on a single sensor image. Therefore, it is possible to impose a uniform distribution on τ, i.e.:

$$\tau = U[\tau_{min},\tau_{max}] \tag{3.12}$$

The accuracy of the displacement estimate $\tilde{\tau}$ is of primary importance when evaluating sensor performance. Defining $\tilde{\tau}_{err}$ as the error in the measurement:

$$\tilde{\tau}_{err} = \tilde{\tau} - \tau \tag{3.13}$$

the performance of the system can then be gauged by looking at the statistics of $\tilde{\tau}_{err}$. To measure the statistics of the estimate error, an appropriate range of τ values is first chosen. Correct implementation of the algorithms ensures:

- First, the estimate is unbiased (i.e. zero mean, or $\bar{\tau}_{err} = 0$), and
- Secondly, in the absence of noise, the estimates will lie in a range of one sample spacing, i.e. ΔX, of the true value.

The basic modelling approach focuses on small excursions from the boresight, hence it is sufficient to consider that τ is uniform on $\left[-\frac{\Delta X}{2}, \frac{\Delta X}{2}\right]$.

The variance, however, provides a quantity that is useful for comparing performance. The variance of the error σ^2_{err} can be calculated as:

$$\sigma^2_{err} = E\{\tau^2_{err}\} + \bar{\tau}^2_{err} = E\{\tau^2_{err}\} \tag{3.14}$$

Therefore, the primary performance metric, the effective resolution δ_{eff} is evaluated as follows:

$$\delta_{eff} = \frac{\sigma_{err}}{\Delta X} \tag{3.15}$$

This quantity normalizes the standard deviation of the error by the pixel size. Thus, the performance of the sensor is expressed in terms of the number of pixels worth of displacement that can be resolved. The smaller the value, the greater the super-resolution performance.

Another useful metric for comparison is *performance gain* G. This can be used to make a qualitatively meaningful comparison of algorithms, illumination patterns, and noise levels, or a combination of the above. The performance gain of trial B with respect to trial A is defined as:

$$G_B = \frac{\delta_{eff_A}}{\delta_{eff_B}} \tag{3.16}$$

Please note the subscripts in this expression. This definition was chosen to ensure that the quantity represented by it matches the intuitive understanding that a high gain represents good performance.

3.6 Summary

The analytical sun-sensor model that can be used for processing the displacements in illumination pattern was developed. The baseline parameters for the model was derived by comparing it to the SS-256 sensor. The implementation of different super-resolution techniques for specific peak-patterns and situations of noise was analyzed. A performance metric called the effective resoltuon was derived in this section to quantitatively assess the performance of super-resolution algorithms in estimating the displacement of sun illumination pattern.

Chapter 4

PERFORMANCE EVALUATION

In this chapter the performance of super-resolution processing techniques are evaluated. One-slit and two-slit detector illumination patterns are examined in the presence of increasing system noise. A comparitive study on different illumination patterns are conducted to observe various mask design trends. These tests can be helpful in providing quantitative comparisons of algorithm performance and assess how simple sensor redesign can improve the net system performance. The main goal of this chapter is to evaluate:

- Performance gain of parametric algorithms relative to conventional methods, in improving the angular accuracy of digital sun-sensors.
- Simple changes to the illumination pattern that can help redesign the aperture mask of the sensor.

4.1 Effects of System Noise

The first set of tests evaluated algorithmic performance as a function of noise strength for different illumination patterns. In laboratory testing, the observed image-to-image standard deviation with the SS-256 sensor was approximately 0.3% of the peak intensity. Since this characteristic level is very low, the analytical sun-sensor model includes only an AWGN term with zero mean and variance, σ_n^2. The pixel noise was varied from 0% to 3% of the peak illumination. Tests performed at noise levels near 3% may be unrealistic in true sensor images, but they are useful in the analysis of generic image degradation.

4.1.1 Baseline Pattern

The narrow, single-peak pattern is considered as the baseline pattern. The effective resolution (δ_{eff}) values of peak-detection, centroiding, linear-phase and eigenanalysis processing techniques against increasing noise levels are shown in Fig 4.1.

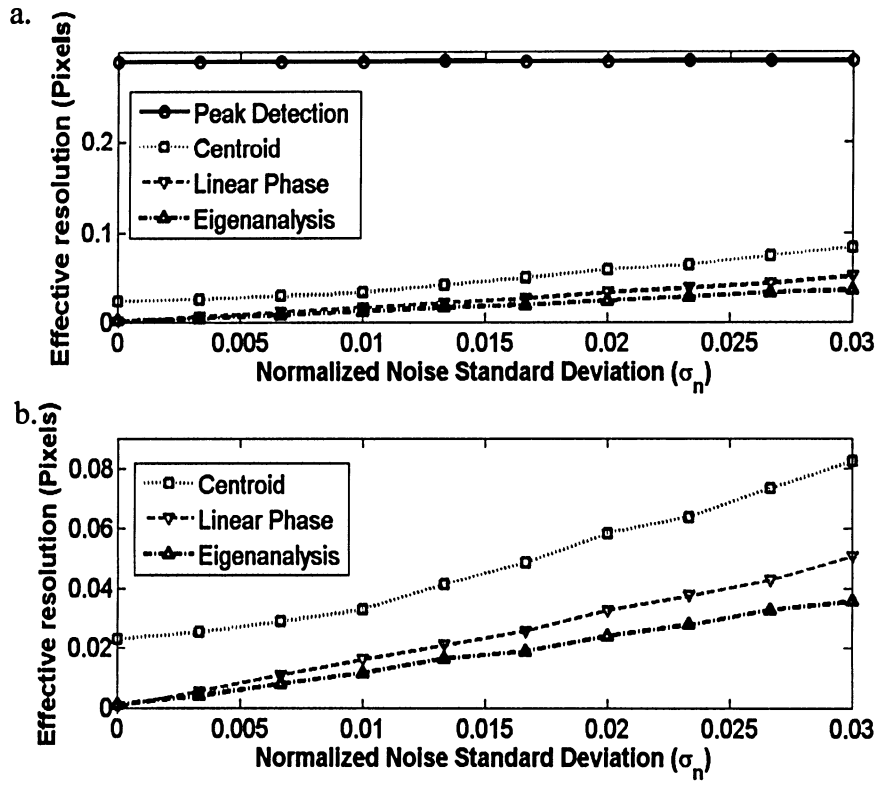

Figure 4.1 Variation of effective resolution with increasing noise for narrow, single-peak illumination. (a.) Full view, (b.) Detailed view.

The invariant performance of peak-detection algorithm (Fig 4.1.a) may be puzzling, but the result is entirely consistent with the definition of δ_{eff} in Section 3.5. Considering a noise-free case, an expression for δ_{eff} can be made directly:

$$\delta_{eff} = \frac{\sqrt{\int_{-\Delta X/2}^{\Delta X/2} \frac{X^2 dX}{\Delta X}}}{\Delta X} = \frac{1}{\sqrt{12}} \cong 0.28 \qquad (4.1)$$

This is the value observed during the tests. The simplicity of the algorithm confers the observed noise immunity. Moving away from the central peak creates a sharp drop in the pixel illumination. Hence, it becomes increasingly unlikely that random noise will cause the algorithm to mis-identify the peak.

The other algorithms are very effective at low noise levels, and the performance of parametric methods is particularly compelling (Fig 4.1.b). Eigenanalysis yields the best results when compared to any of the other algorithms over the entire range of noise values. Although noise causes the performance of the linear phase algorithm to degrade faster than eigenanalysis and centroiding, its low-noise performance is excellent. The combination of modest computational cost and good performance makes this algorithm attractive.

Considering the centroiding algorithm as the conventional 'smart' approach, the relative advantage of using one of alternate algorithms can be examined. This effect is shown in Fig 4.2. This plot shows a ratio of δ_{eff} values of the centroiding algorithm to the other three candidates. Using the equation of gain in (3.16), the relative gain of peak-detection, linear phase, and eigenanalysis algorithm with respect to centroiding can be calculated.

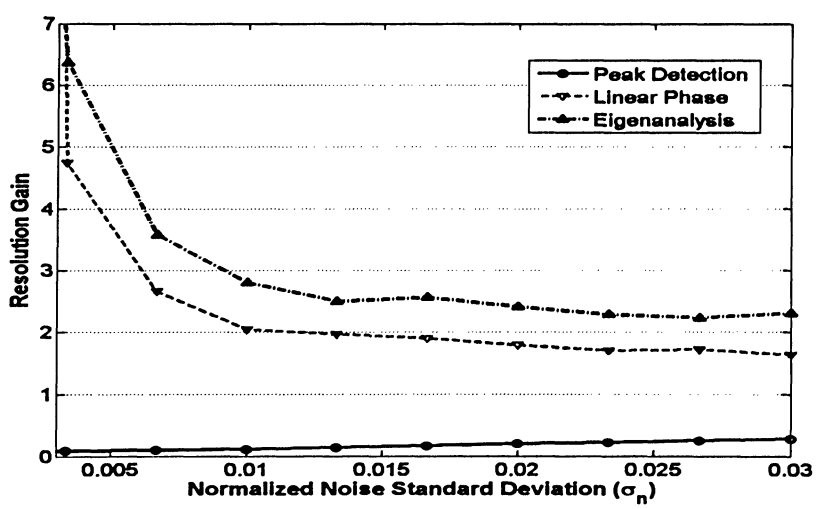

Figure 4.2 Performance gain for narrow, single-peak illumination pattern, relative to the centroid algorithm. Values over unity represent performance better than the centroiding algorithm.

The performance of the centroiding and parametric algorithms changes at similar rates. Therefore, as the denominator term increases, the relative advantage of the parametric processing approach is gradually reduced. With zero-noise, the estimation accuracy of parametric algorithms is nearly perfect. These points have been omitted from the graph to preserve a meaningful vertical scale. At 0.3% noise the parametric algorithms demonstrate gains of around 4.9-6.5. Laboratory experience with the SS-256 sensor suggests that low noise (~0.3%) operating conditions are typical. Therefore, a relative improvement of more than four, is substantial.

4.1.2 Comparative Trends

The tests performed in this section considered the four permutations of narrow or wide, and one or two-peak detector illumination patterns. Each test can be assigned an identifier as explained in Table 4.1.

TABLE 4.1 Definition of Comparative Illumination Patterns

Identifier	Reference	X_{max}
N1	Narrow, one-peak pattern	25
N2	Narrow, two-peak pattern	50
W1	Wide, one-peak pattern	25
W2	Wide, one-peak pattern	50

Treating the narrow, single-peak (N1) performance of the four algorithms as a baseline, the effect of the different illumination patterns can be examined. Therefore, with the help of (3.16), the relative gain of N2, W1, and W2 with respect to N1 pattern can be calculated for peak-detection, centroiding, linear-phase, and eigenanalysis algorithm.

The performance gain plots for each algorithm are shown in Fig 4.3.

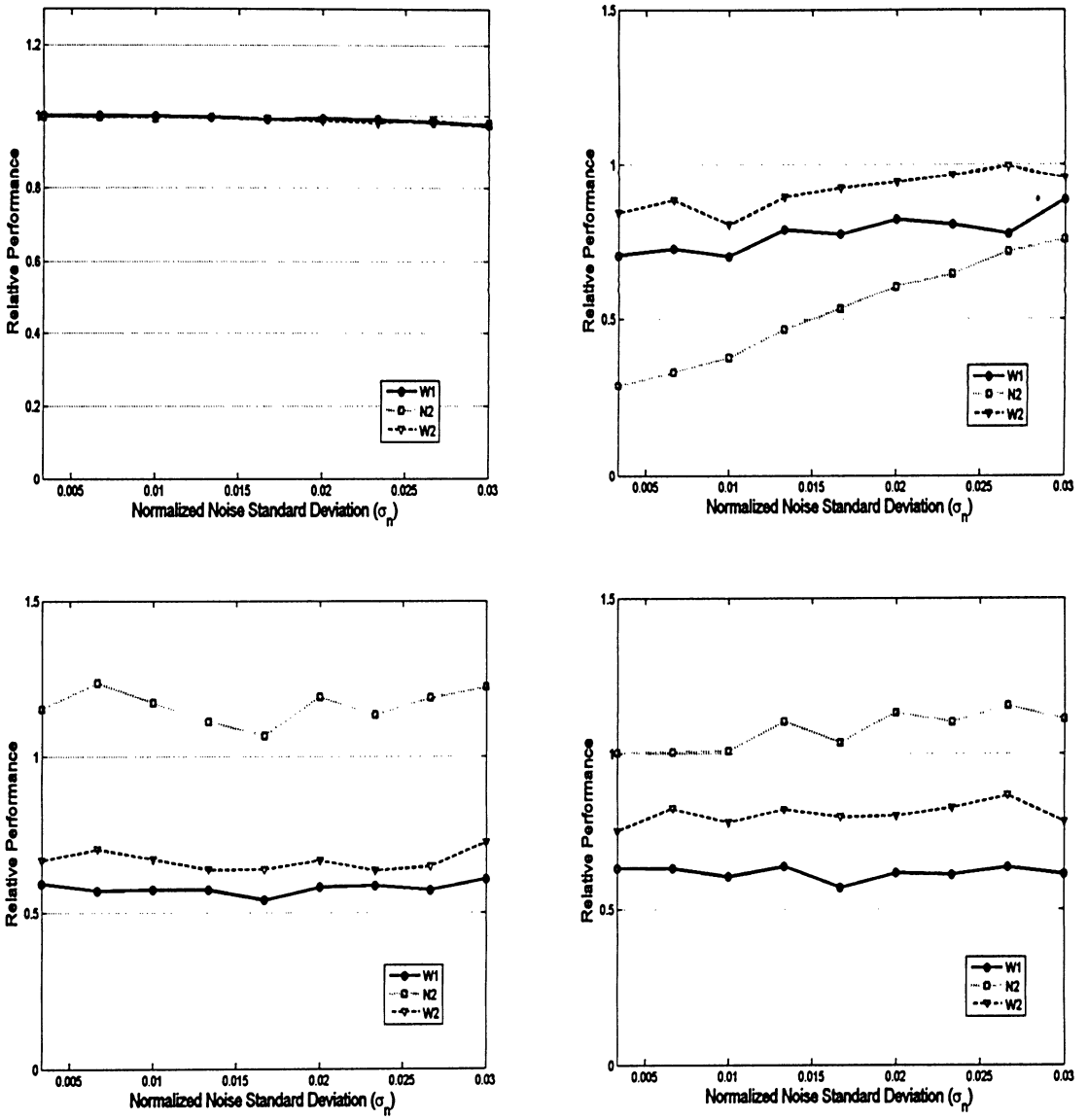

Figure 4.3 Illumination pattern effects on performance gains for peak-detection (a.), centroiding (b.), linear-phase (c.), and eigenanalysis (d.). Each algorithm is compared to its narrow, one-peak results.

The following observations can be made about these results:

1. Peak-detection shows little variation in performance with changing illumination patterns. This was also observed when the illumination patterns were tested separately with increasing noise.

2. Throughout the test regime, from Fig 4.3.(b), the centroid algorithm appears to favour wide peaks compared to narrow peaks. This could be attributed to the performance of centroiding algorithm for narrow, one-peak illumination pattern (N1). It was shown earlier that the centroiding method performed the worst for the N1 test.

3. In the case of parametric algorithms (linear-phase and eigenanalysis), the narrow peak patterns outperform wide peak patterns by a factor of two (approximately). This shows that, these algorithms are worth considering since they demonstrate gains significant enough to justify the added computational requirements over the conventional centroiding processing technique.

4. Generally, N2 test exhibited the best performance, followed by N1, W2, and finally W1. Thus, the narrow peaks outperform wide peaks, and double peak detector illumination patterns perform better than single peak illumination patterns of the same width. This suggests that "good" patterns are good for any algorithms.

This preliminary exploration of illumination pattern and algorithm performance provides insight into possible sensor redesign strategies. First, it is observed that parametric algorithms promise substantial performance gain over traditional algorithms under favorable conditions of noise. Next, it is clearly visible that the peak width and number of peaks, both, affect the effective sensor resolution. Of these, the latter seems to be the more important factor in improving sun-sensor performance. Overall, it was observed that the performance gains for the four algorithms are fairly flat; they are not very sensitive to increasing noise. This suggests, albeit weakly, that illumination patterns do not have to be optimized with respect to noise.

The final observation is,

$$N2 > N1 > W2 > W1 \tag{4.2}$$

4.2 Mask Design Trends

In this section, the purpose of the tests are to elaborate on the general trends uncovered in the previous sections (Section 4.1). A rigorous optimization of sun-sensor illumination patterns will be discussed in Chapter 5. In Section 4.1.2, it was shown that the N2 trial performed better than the N1, and that the N1 usually performs better than W1. Therefore, three set of tests will be considered in this section:

1. Effect of the number of peaks.
2. Effect of varying peak-width for one-slit illumination patterns.
3. Effect of changing the native resolution of the sensor.

4.2.1 Peak-width Variation - One Slit Illumination Pattern

The effective resolution of each algorithm relative to a single peak of varying width, is shown in Fig 4.4. The width of the peaks was varied from about 2% of the field to 35%, and 0.3% sensor noise was used in the simulation.

The peak-detection performance is unchanged for relatively narrow peaks. As the peak width increases, the relatively broad extent of the peak increases the likelihood that noise will disturb the algorithm's estimate of the peak location. Fig 4.4.(b) highlights the performance of the centroiding, linear-phase and eigenanalysis algorithms. The narrow-peak cases from the previous section are reflected in the left-most points on the graph.

The centroiding algorithm shows better performance for narrow-peaks; starting quite low and gradually worsening as the width increases. The most remarkable changes occur with the parametric algorithms. For narrow peaks, almost perfect localization is achieved. The eigenanalysis algorithm and linear-phase demonstrates similar width sensitivity (i.e. lowest slope), when compared to other algorithms under consideration.

The performance of each of these algorithms worsens as the peaks widen. From the perspective of the centroiding algorithm, wide peaks will have more noise content in the

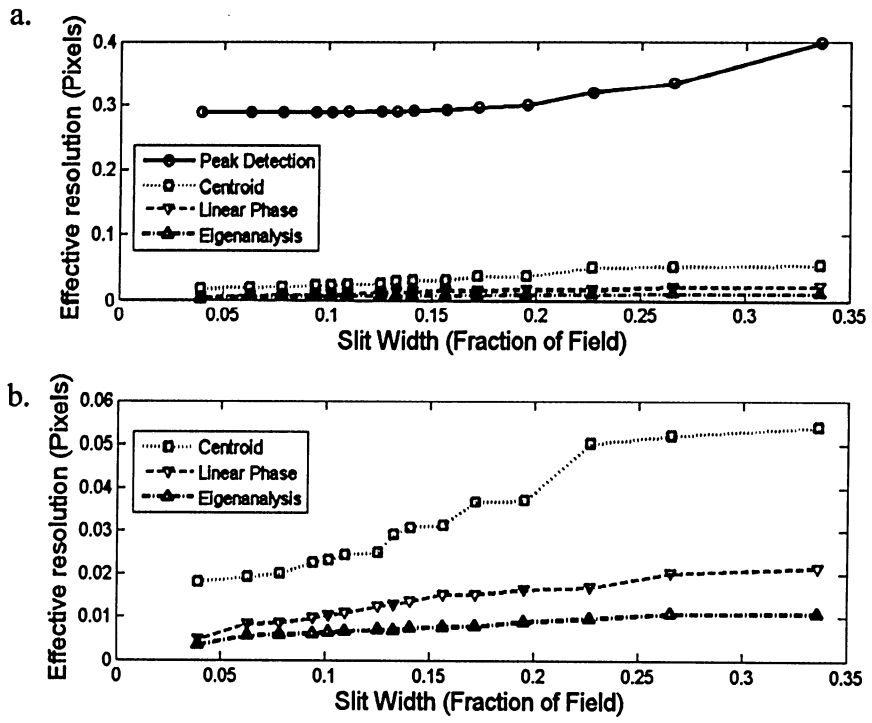

Figure 4.4 Effective resolution as function of Slit Width, $\sigma_n = 0.003$.

calculations and therefore the effective resolution will increase when the peak window is wide. For the linear-phase algorithm, wide peaks will have narrow transforms, hence the linear region of the phase function will shrink.

Considering the performance of centroiding algorithm as the conventional "smart" approach, the relative advantage of using one of the alternate algorithms can be examined (Fig 4.5). This plot shows the performance gain of the algorithms with respect to centroiding. Although the data is erratic[1], there is a suggestion of local minima for both eigenanalysis and linear-phase algorithms. This high gain near the very narrow and very wide extremes is caused by a drop in the centroid performance, and not by an improvement in these algorithms.

For narrow peaks, the centroid algorithms does not get enough samples to work with in the centroid window. This causes a bias in the estimates of τ. For wide peaks patterns, as more

1. This fluctuation is caused by sensitivity to centroid window size, k.

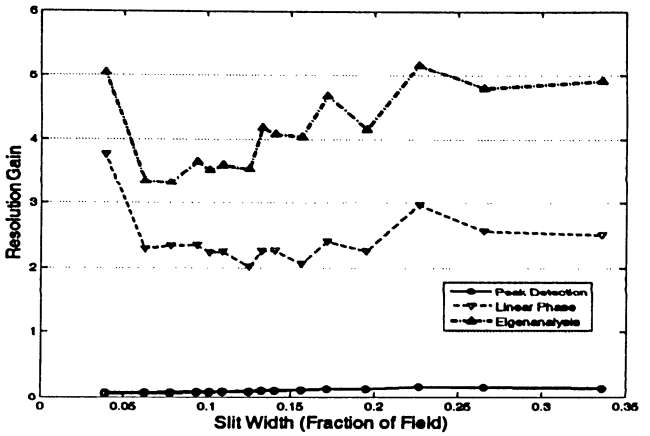

Figure 4.5 Performance gain as a function of peak width, relative to centroiding.

pixels are included in the localization, more noise is introduced into the calculations. This affects the performance of the algorithm. Therefore, this algorithm performs at its relative best in the middle region.

Fig 4.6 shows the performance gains of each algorithm with respect to the narrow-peak resolution. It can be clearly seen that wide peaks generally degrade performance.

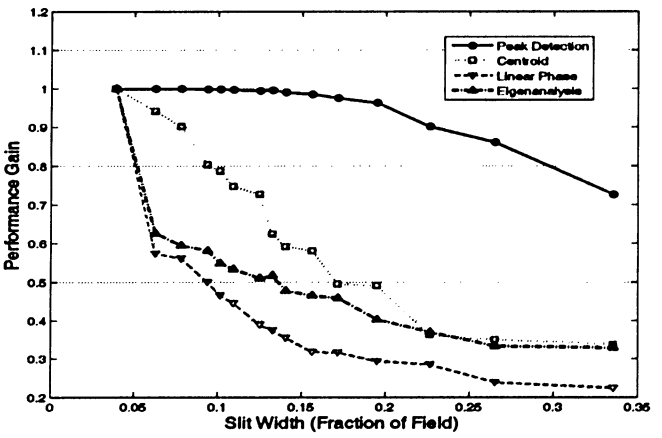

Figure 4.6 Effect of peak-width on algorithm performance. The performance gain for each algorithm is calculated with respect to the algorithm's narrow-peak (X_{max} = 50) resolution.

From the plots shown above, it can be observed that there is little reason to alter the peak-width on the illumination pattern. Although a very wide peak seems to offer good performance gain, the absolute performance suffers. Narrow peaks offer superior performance for the algorithms under consideration.

4.2.2 Multiple Peaks

In this section, a complementary trend to the previous set of simulations is explored. The narrow-peak detector illumination pattern is retained, and the tests are conducted by altering the number of peaks. Symmetric illumination patterns were generated for values of N_p between one and ten, and the sensor noise was normalized to 0.3%.

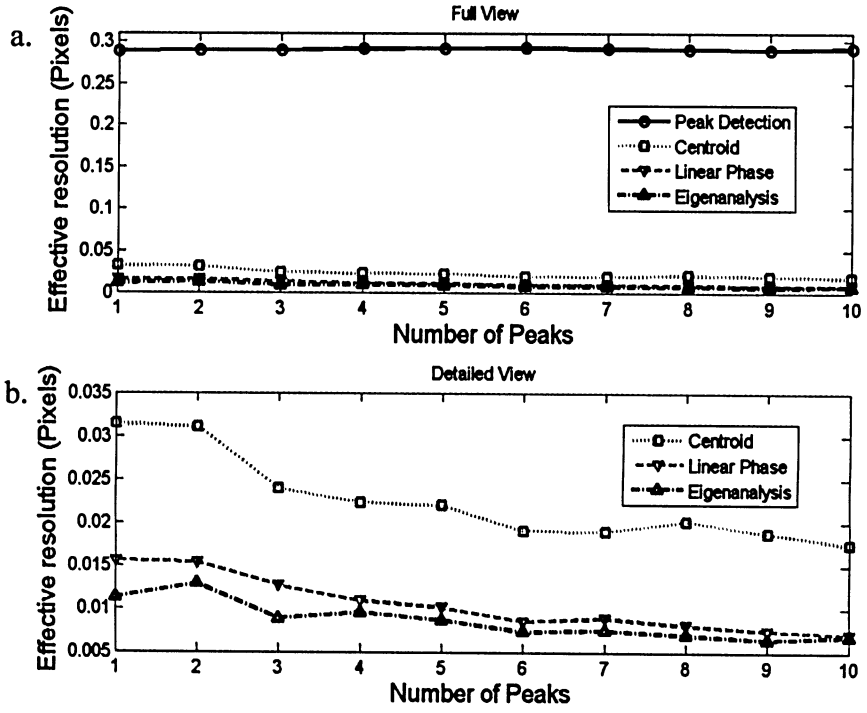

Figure 4.7 Effective resolution as a function of number of peaks.

The effective resolution obtained from the multiple peak analysis is shown in Fig 4.7(a). The effective peak-detection resolution remains constant as the number of peaks increases. Since

the algorithm uses a very simple approach, it gains little from the additional peaks. The centroiding algorithm shows consistent improvements in performance as N_P increases. The two parametric algorithms remain close together in performance (Fig 4.7(b)). Eigenanalysis remains the best choices in terms of raw precision.

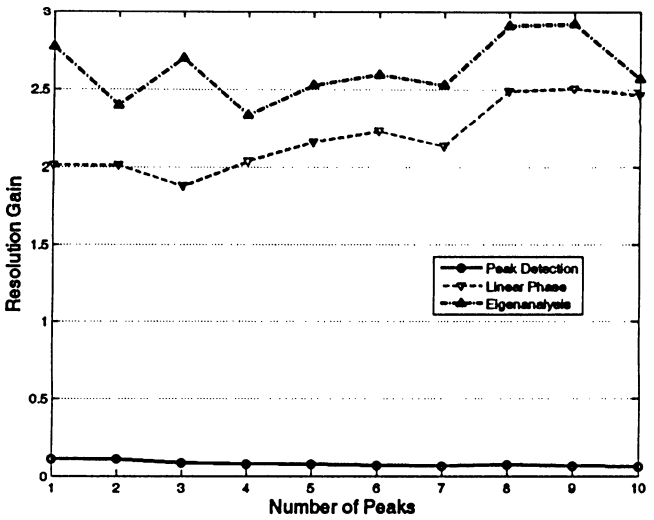

Figure 4.8 Resolution gain (relative to centroid algorithm) as a function of number of peaks.

Fig 4.8 shows performance gains with respect to the centroid algorithm. The performance gain plot for the algorithms shows that the linear-phase and eigenanalysis algorithms outperform the centroid algorithm by about the same factor, regardless of the number of peaks in the illumination pattern.

Finally, the effective resolution of each algorithm relative to its own one-peak performance is considered in Fig 4.9. Two important observations can be made.

- First, the move to a ten-peak pattern yields a gain of about two for each of the algorithms except for peak-detection.
- Second, the linear-phase algorithm seems to benefit a little more than the others from this change.

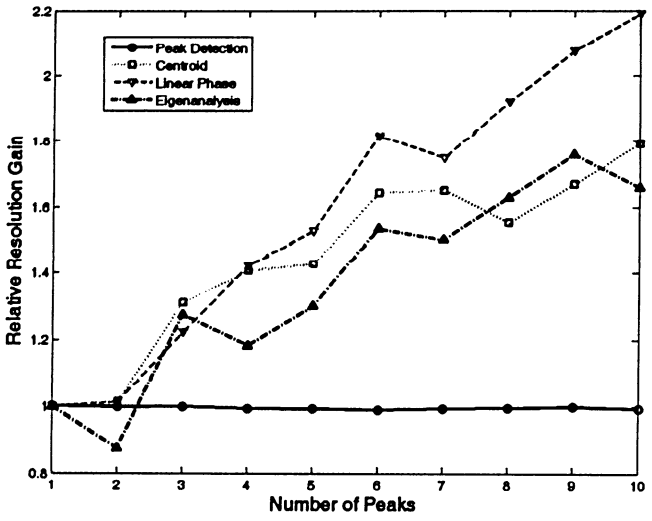

Figure 4.9 Effect of number of peaks on algorithm performance. The relative gain of each algorithm is calculated with respect to the algorithm's single-peak resolution.

4.2.3 Native Sensor Resolution

In the previous section, wide-peak illumination patterns were found to degrade performance. Despite the lacklustre performance, it is useful to investigate how the more modest changes in peak-width will effect sensor performance. Changing the native resolution of the sensor is another way of increasing the peak-width. A sensor capable of creating such an illumination pattern on the detector would require non-trivial changes to the geometry (i.e. z_s must increase). If z_s increases substantially, the field-of-view will shrink. In a real sensor, altering the peak width is difficult to do without compromising on other performance characteristics like sensor field-of-view. One method does remain that may help capitalize on the potential of parametric algorithms: improving the native resolution of the sensor. Changes to the detector array could alter the perceived width of the illumination pattern.

Altering the native sensor resolution requires the replacement of the detector array. Thus, a detector of the same physical dimensions will house a greater or lesser number of pixels. This results in a change to ΔX, but X_{max} remains the same. As the number of pixels rises (and the pixel size shrinks), the narrow peak will be imaged with a greater number of samples. This

change is made with greater reluctance than earlier changes to the processing algorithm and sensor geometry since the costs involved will generally be higher.

Adding pixels to the narrow pattern sensor gives the results shown in Fig 4.10.a. Each time the pixel size is halved, the peak is resolved by double the number of pixels. Over this range of pixel sizes, the effective resolution of centroiding, linear-phase and eigenanalysis all improve with increased peak definition (their performance is similar as well). Not only is the native resolution improved by using smaller pixels, but the illumination displacement can be measured to a smaller fraction of a pixel. Since the peak-detection algorithm uses only a single pixel to generate $\tilde{\tau}$, its performance remains constant. For other algorithms, increasing pixel size (lower resolution sensors) impairs the effective resolution, but decreasing the pixel size before unity has little effect.

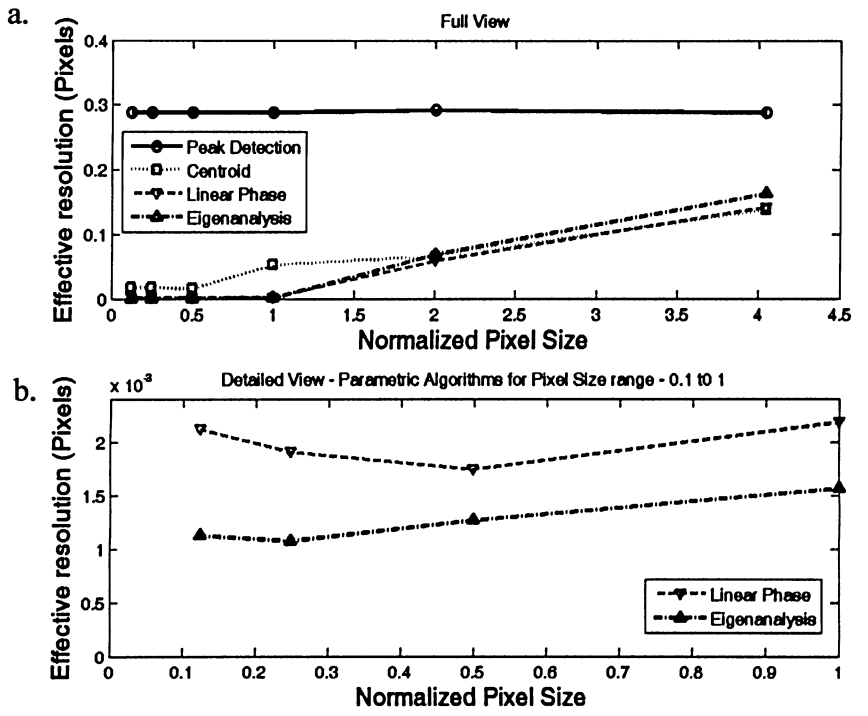

Figure 4.10 Effective resolution as function of pixel size (σ_n = 0.003, narrow pattern). Pixel size has been normalized to that of 256-element array. Note that the points to the right indicate detectors with fewer pixels.

There seems to be a shallow optimum (Fig 4.10.b) for the parametric algorithms for pixel sizes between 0.25 and 0.50, but the effect is not very pronounced. Thus, reducing the pixel size allows to resolve smaller absolute shifts, but the sub-pixel performance remains relatively unchanged. Increasing the pixel size is doubly harmful since it is possible to see a degradation in both sub-pixel resolution, compounded by the increase in pixel size.

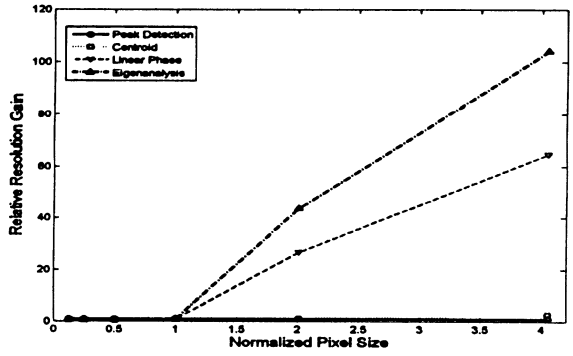

Figure 4.11 Relative performance as function of pixel size (σ_n = 0.003, narrow pattern). Effective resolution for each algorithm is normalized to the algorithm's 256-pixel result.

Fig 4.11 shows the algorithm's performance relative to its 256-pixel trial. The parametric algorithms demonstrate an increase in performance as the pixel size increases. Peak-detection and centroiding algortihms fare worse when compared to parametric algorithms. Continually increasing the number of pixels in the array was impractical. Besides running up against the limits of detector technology, certain algorithms were detected to be significantly slower when operating on longer data signals.

Fitting 2048 pixels into a 16mm array requires a pixel pitch of less than 8μm; this is close to the limit of current commercial technology[1]. In such cases, it is also possible to just window the data around the peak. The pixels that contain no data can be eliminated. Nevertheless, it was important to evaluate the limits of the performance trend.

1. For a comprehensive, but somewhat dated example, [Eid et al, 2001] provides many examples of radiation tolerant sensors. An informal survey of contemporary cameras and pixel arrays revealed few with pixel pitch finer than 8μm.

Some noise sources (e.g. reset noise, amplifier noise, and quantization noise) do not scale with pixel size. Therefore, changes to the array may require adjustments of the sensor integration time or the use of a different natural-density filter to maintain an equivalent signal-to-noise ratio (SNR). If it is unable to compensate for these effects and the SNR drops with pixel size, then the system performance is expected to degrade with smaller pixels. In this situation the optimal pixel size may be more significant.

4.3 Performance Conclusions

In this chapter, it was shown that under low-noise operational conditions, linear-phase and eigenanalysis algorithms yield sizeable improvements in sun displacement estimates. Provided that these improvements hold across to the full sensor field-of-view, parametric algorithms represent a promising avenue for greatly improving sensor performance at the cost of modestly increasing computational requirements. The current standard approach, centroiding, requires next to nothing in terms of processing power. However, the gains from the parametric algorithms are substantial enough to validate this approach as a concept worthy of further study.

The results presented in this chapter suggested that parametric algorithms have the potential to greatly enhance the effective resolution of the modelled sensors. In a laboratory experiment, these algorithms were applied to image data collected from the SS-256 sensor, and the tests proved that these improvements were physically realizable and not simply a product of the simulation or modeling process [Enright & Godard, 2005]. The agreement in results suggests that despite simplifying assumptions, the sensor model is sufficiently accurate for predicting algorithm performance.

Although this chapter demonstrated some variation of performance with illumination pattern, the pattern selection process has been *ad hoc.* The mask design trends observed are promising enough to promote further evaluation of sensor re-design. Systematic optimization of the aperture pattern will be evaluated in Chapter 5.

Chapter 5

MASK OPTIMIZATION

Performance of a sun-sensor can be increased by redesigning several aspects of the sensor system. In Chapter 4, it was shown that changes to the illumination pattern in a digital sun-sensor can dramatically improve the resolution of the device. In this chapter, *Genetic Algorithms* (GAs) will be used as a heuristic to optimize the illumination pattern for a single-axis digital sun-sensor. Thus, the optimized pattern will be selected based on the degree to which it improves sensor resolution. Changes to the detector illumination pattern can be implemented by altering the sensor's aperture mask. Since this is a superficial change to a passive component, manufacturing costs will not increase.

After providing some background information on GAs, design of the optimizer algorithm will be explained, including a description about specific genetic operators used for mask optimization. Following a discussion of results obtained from GA optimization procedure, the effect of super-resolution algorithms on the performance of the optimized pattern will be examined.

5.1 Fundamental Approach

Genetic Algorithms are a class of searching processes based on the laws of natural selection and genetic evolution. GAs were first proposed by John Holland [Jackson & Carpenter, 2004], as a means to find good solutions to problems that were otherwise computationally intractable. Because of its simplistic implementation procedure, GA is used widely in AI-

hybrid systems for real-world applications [Goldberg, 1989], direction-of-arrival estimation [Li & Yi, 2004], and many other practical problems in science, engineering and industry. Genetic Algorithms differ from other traditional optimization procedures in several ways [Jackson & Carpenter, 2004]:

- GAs work on the coding of problem parameters, not on the parameters themselves.
- GAs search a population of points in the solution space, not a single point. Thus it could avoid being trapped in a local minimum. GA is also free of assumed starting point.
- GAs use objective function metrics to guide the search process, not derivatives or other auxiliary knowledge of the solution space.
- GAs use probabilistic (stochastic) transition rules to traverse the solution space, not deterministic rules.

A simple GA consists of three basic operations: Selection, Genetic Operation, and Replacement. A typical GA cycle is shown in Fig 5.1

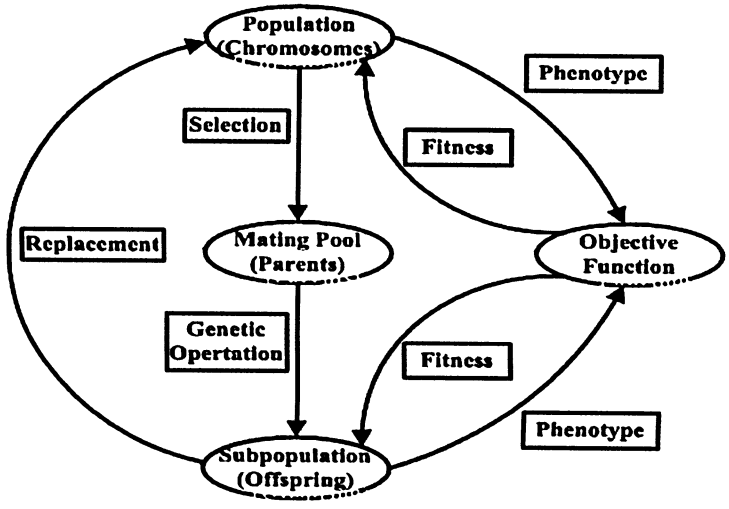

Figure 5.1 GA Cycle [Tang et al, 1996].

The basic process begins by a randomly generated population of chromosomes, which are fed into the objective function through which GA carries out a fitness-based selection and recombination to a new generation of successor population. During recombination, the genetic material in the parent chromosomes are selected based on the fitness score and recombined to form a subpopulation or child chromosomes, and these are passed on to the successor population. This is an iterative process through which various generations are evolved until some stopping criterion is specified, and an *optimal solution* is reached based on increasing fitness score.

A GA is constructed from a number of distinct components. The main components are chromosome encoding, fitness function, selection, recombination, and the evolution scheme.

5.1.1 Chromosome Encoding

The population comprises of a group of *chromosomes* from which candidates can be selected for the solution of a problem. A particular position in a chromosome is referred to as a *gene* and the value occurring at that point in the chromosome is referred to as the *allele value*. The classical GA uses a bit-string (Discrete) representation to encode solutions. Bit-string representation consists of a string of genes whose allele values are characters from the alphabet $\{0, 1\}$. The interpretation of this string is entirely dependant on the specifications of the problem. The GA toolbox in MATLAB also allows the use of real numbers in vector form (Continuous representation). The exact meaning of any chromosome for a particular application is encoded only in the second part of the GA, the fitness function.

5.1.2 Fitness Function

Given a specific problem to solve, the input to the GA is a set of potential solutions - "*chromosomes*" - to that problem encoded in some fashion, and a metric called a *fitness function* that allows each candidate to be quantitatively evaluated. The fitness values of all the chromosomes are evaluated by calculating the objective function in a decoded form (phenotype). The objective function (or fitness function) is the main source for providing the

mechanism that evaluates the performance of each chromosome. Basically the fitness function takes a chromosome as input and produces a number, or set of numbers, as a measure to the chromosome's performance. A genetic algorithm is only as good as its fitness metric. Without this component, there would be no other way for the algorithm to differentiate the good solutions from the poor ones.

5.1.3 Parent Selection

Parent selection uses the fitness values to select the chromosome in a GA population that provides the best solution. The chromosomes with higher fitness value are prone to be selected against those with lower fitness score because they tend to receive higher number of offsprings. Thus, these individuals have a higher chance of surviving in the subsequent generation. This selective procedure evolves highly fit solutions. Even the highly fit chromosomes could be selected more than once and also can be recombined with themselves. Effective selection is achieved by many ways, but the most famous among them is the Roulette Wheel Selection, which is based on proportionate scheme [Goldberg, 1989]. The procedure is as follows:

- Sum the fitness of all population members, named as total fitness.
- Generate a random number between 0 and total fitness n.
- Return the first population member whose fitness added to the fitness of the preceeding population members is greater than or equal to n.

There are many different selection schemes. Tournament Selection first selects two chromosomes with uniform probability and then chooses the one with highest fitness. Truncation Selection simply selects at random from the population having first eliminated a fixed number of the least fit chromosomes [Back et al, 1997]. Random Stochastic Selection explicitly selects each chromosome a number of times equal to its expectation of being selected based on the fitness proportional method.

5.1.4 Genetic Operation

Genetic operation or *recombination*, is the process by which chromosomes selected from a source population are recombined to form members of a successor population. This stage involves two components, *Crossover* and *Mutation*. Crossover operator combines subparts of two parent chromosomes to produce offspring that contain some parts of both parents' genetic material. A single point crossover (Fig 5.2) defines a single cross point where the two parent chromosomes can be split and the two chromosomes beyond this point are exchanged to form the offspring. A multipoint crossover (Fig 5.3) is similar to single point crossover, except that m cross points are chosen at random and the child chromosomes are constructed from the allele values of the two parents, interchanging at each crossover point.

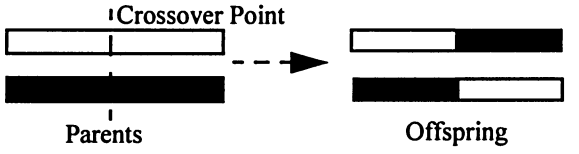

Figure 5.2 Example of single-point crossover.

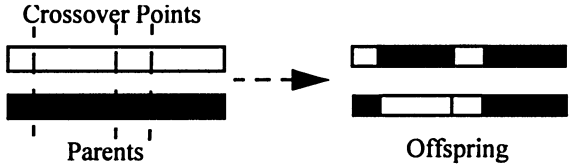

Figure 5.3 Example of multipoint crossover (m = 3).

Mutation is an operator that introduces variations into the chromosome. These variations can be global or local. Basically it acts on an individual chromosome and flips one or more allele values. In the case of bit-string chromosomes, a normal mutation operator randomly alters the value of the string position. An example of mutation on the fourth bit is shown in Fig 5.4.

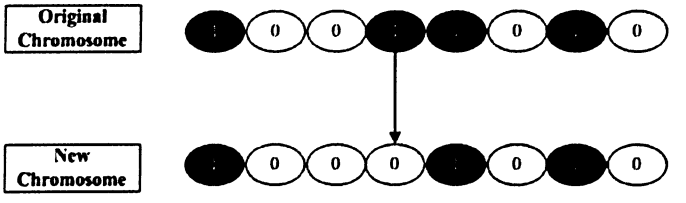

Figure 5.4 Example of bit mutation on the 4th bit .

5.1.5 Evolution

The genetic operations helps recombination and the resultant chromosomes are passed into the successor population. The processes of selection and genetic operation are iterated until a complete successor population is obtained. This leads to the formation of a new source population or the next generation. The GA is then iterated through a number of generations until a stopping criteria specified is reached. Two representative strategies are used for old generation replacement, Generational Replacement and Steady State Reproduction [Tang et al, 1996]. In generational replacement, each population of size n generates an equal number of new chromosomes to replace the entire old chromosome. In steady state reproduction, only a few chromosomes are replaced once in the population to produce the succeeding generation. These are called the evolutionary schemes and they form a very important aspect of GA design.

In general, a top-level description of simple GA will be as follows:

- Step 1 - Randomly generate an initial population $X(0) = (x_1, x_2, x_3, ..., x_N)$;
- Step 2 - Compute the fitness $F(x_i)$ of each chromosome x_i, in the current population $X(t)$;
- Step 3 - Create new chromosomes $X_r(t)$ by mating current chromosomes, applying mutation and crossover during mating;
- Step 4 - Delete numbers of population that provide low fitness scores, to make room for the new chromosomes;
- Step 5 - Compute the fitness of the new set of chromosomes $X_r(t)$ and insert these into the population;
- Step 6 - Check for stopping criteria;
- Step 7 - If stopping criteria met, then stop and return the best chromosome, or else go to Step 3 and re-iterate.

5.2 Optimizer Algorithm Design

A mathematical model of sun-sensor performance is necessary to evaluate the impact of illumination pattern changes. A standard data model for optimizing the illumination pattern can be formulated based on the design of an analytical sensor model (Section 3.3). A few practical observations can be made about the image synthesis.

5.2.1 Chromosome Pattern

In this study, a binary sequence (0-1 sequence) is used to represent the chromosome, P_M. The peak-position and peak-width was encoded in a single chromosome. A pattern with M peaks can be denoted by P_M, where P_M is the tuple:

$$P_M = \{k_1, w_1, \ldots, k_M, w_M\} \tag{5.1}$$

The elements of the tuple that define the pattern are:

- Peak Position k_i. This defines array index of the centre of the peak i.
- Peak Half-width w_i. This quantity is the half-width, in pixels where the peak intensity falls to 10% of the maximum value.

These variables represent the population that will be optimized by GA.For the initial case of a one-peak illumination pattern, there are a total of 11 bits in a chromosome string. The first 8 bits are used to calculate the peak-position, and the consequent 3 bits corresponds to peak-width. Therefore, for a ten-peak illumination pattern, there will be a total of 110 bits to evaluate the ten peak-positions and their respective peak-widths.

A separate optimization was performed for each value of M. This removes the need for the chromosome to represent the number of peaks explicitly. This approach improves solution coverage and convergence.

5.2.2 Fitness Scaling and Selection

The *linear-phase* parametric algorithm will be used to evaluate the performance of each candidate illumination pattern. Parametric super-resolution techniques derive an advantage over conventional processing techniques from *a priori* knowledge of the expected illumination pattern at the detector. One of the main advantage of these algorithms is their tolerance of random noise and interfering signals. Consequently, these algorithms permit precise localization of the sun in the sensor image. The performance of the sun-sensor is expressed in terms of the number of pixels worth of displacement that can be resolved. This is also called the *effective resolution* δ_{eff}. This will be the quantity minimized by GA, to optimize the illumination pattern.

A *Rank-based* fitness scaling is used for this proposed model. This is preferred over other methods because of its ability to produce successive generations with the best individual chromosomes [Goldberg, 1989]. Rank-based fitness scaling also helps converge to an optimal solution faster than other fitness schemes.

A *Stochastic Uniform* parent selection scheme is used for this model to emulate the survival of the fittest mechanism. This allows the fitter chromosome to receive higher number of offspring and thus a higher chance for that chromosome to survive in subsequent generations. Roulette wheel selection was not used for this model, since it is mainly used to implement a proportionate scheme.

5.2.3 Crossover and Mutation

A *Scattered Crossover* operation was proposed for this model so that the operator generalizes the scheme to make every locus a potential crossover point. A crossover probability of $P_c = 0.8$ is used for this model.

The variations into the chromosome was introduced using a *Uniform Mutation* function. Since the number of genes in a chromosome in this case range from 11 to 110, a mutation probability of $P_m = 0.5$ was used. This number is relatively high compared to typical mutation

rates, but with a large population size of 500, the probability of mutation needs to be high enough for better results and faster convergence.

5.2.4 Termination Criteria

The convergence criteria was set by the maximum number of generations. Considering a population size of 500 and a maximum chromosome size of 110 bits, the GA is expected to converge within 800 generations. Therefore a $G_{max} = 1000$ was employed in this GA. The algorithm was also set to terminate if the cumulative change in the fitness function value over stall generations (100) is less than 1×10^{-6}. This is an important criteria because if GA finds the minimum value long before G_{max}, then the simulation time can be minimized.

5.3 Optimization Performance Evaluation

This section examines the convergence results of the Genetic Algorithm Optimizer. A set of bounds on the w_i and k_i quantities defines the optimization case. In this study, two cases are considered. These are shown in Table 5.1.

TABLE 5.1 Optimization Cases

Case	Min. w_i	Max. w_i	Min. k_i	Max. k_i
I	1	6	25	235
II	1	6	70	180

To avoid losing peaks off the end of the array as the sun-angle increases, the peaks must be confined to the central region of the array. These two optimization cases consider different sized changes. Case I allows greater generality in the illumination pattern at the expense of a restricted sun-sensor field-of-view ($\pm30°$). Case II restricts the optimization, but does not compromise the sensors's field-of-view ($\pm70°$). The allowable peak widths are the same in both cases.

The test cases for this study varied the number of peaks in an illumination pattern from 1 to 10. Therefore, the role of GA is to find optimal patterns for each of the ten test cases. Two factors must be examined before making a decision on the best detector pattern among the ones selected from the above mention test cases. Of primary concern, the optimal illumination pattern must resolve the sun-angle to the best effective resolution value. A secondary consideration is that, the diffuculty in fabricating the aperture mask of the digital sun-sensor must be considered. To fabricate a single slit mask is easier when compared to manufacturing a ten slit aperture mask. The optimized illumination pattern will then be tested to evaluate the performance of other super-resolution algorithms with increasing system noise.

5.3.1 GA Results

To efficiently evaluate the performance of GA in optimizing the illumination pattern, the optimization results are compared with a two-peak pattern (Section 4.1) similar to that employed on a Sinclair Interplanetary SS-256 digital sun-sensor. This two peak pattern has an effective resolution, $\delta_{eff} = 0.0483$. This value is compared with the fitness scores of the optimized patterns to evaluate the performance gain. Results of the optimizations are shown in Fig 5.5 and Table 5.2.

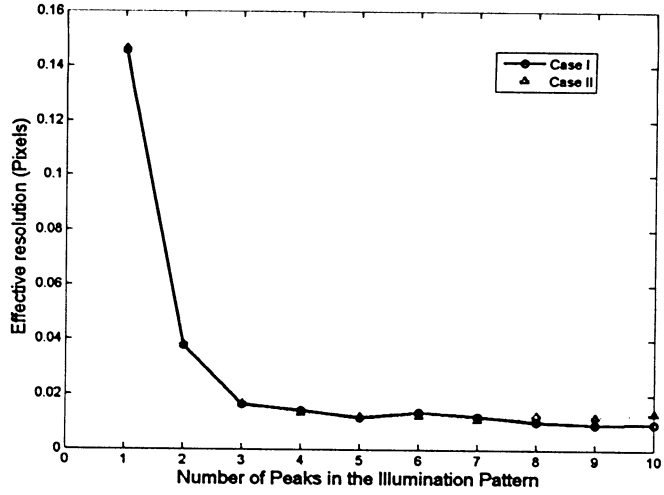

Figure 5.5 Effective resolution obtained from GA for the two test cases.

TABLE 5.2 Comparison of Optimal Patterns with SS-256 Pattern

	Case I		Case II	
M	δ_{eff}	Gain	δ_{eff}	Gain
1	0.14577	0.3	0.14641	0.3
2	0.03795	1.3	0.03841	1.3
3	0.01641	2.9	0.01698	2.8
4	0.01431	3.3	0.01338	3.6
5	0.01167	3.5	0.01234	3.9
6	0.01365	4.0	0.01244	3.8
7	0.01217	4.1	0.01096	4.4
8	0.01010	4.8	0.01255	3.8
9	0.00994	4.9	0.01209	4.0
10	0.00955	5.1	0.01338	3.6

It is clear that the optimization provides an improvement in performance. The optimal two-peak pattern performs similarly to the SS-256 sensor and the performance gain can be attributed to the use of narrower peaks in the optimized pattern. Between one and three peaks, the performance increases dramatically and the two cases are quite similar. From three to six peaks, the performance improvements are smaller, and the two cases continue with similar performance. For patterns containing more than six peaks, the two curves begin to diverge with Case I outperforming Case II. For these patterns, the permitted peak-placement region becomes too crowded.

The three-peak patterns represents a point of diminishing returns. Adding more peaks to the illumination pattern creates progressively smaller improvements in performance. Since the main objective of this study was to minimize changes to the sensor, these three peak patterns were selected as the best candidates for sensor redesign. Since the projected performance gains are very similar, there is little reason to select a pattern that would compromise on the sensor's field-of-view. Thus, the Case II results are most promising.

Table 5.4 shows the various peak-positions and peak-widths of optimal illumination patterns for the two test cases. For test case-1, it is evident that all the peaks are spread out over the

TABLE 5.3 Peak-positions and Peak-widths of Optimal Patterns

Number of peaks	Test Case - I		Test Case - II	
	Peak - Positions	Peak - Widths	Peak - Positions	Peak - Widths
1	248	2	153	2
2	180, 33	1, 2	159, 152	2, 1
3	26, 212, 43	4, 1, 1	157, 177, 71	1, 4, 1
4	223, 141, 127, 101	3, 1, 1, 2	97, 125, 108, 82	1, 3, 1, 2
5	52, 44, 157, 146, 181	1, 2, 3, 1, 1	89, 158, 90, 97, 154	1, 2, 1, 3, 1
6	237, 143, 229, 33, 72, 150	3, 1, 1, 1, 2, 1	134, 95, 170, 160, 123, 81	1, 1, 1, 3, 1, 2
7	227, 27, 96, 242, 37, 30, 168	1, 2, 3, 2, 1, 2, 1	146, 161, 166, 173, 115, 79, 93	1, 1, 1, 1, 1, 4, 3
8	63, 142, 197, 212, 107, 157, 248, 182	1, 1, 1, 3, 4, 1, 1, 2	148, 157, 169, 176, 171, 170, 99, 153	2,1,1,1,1, 3,1,1
9	129, 42, 102, 226, 101, 110, 89, 34, 133	1, 3, 1, 4, 1, 2, 1, 1, 1	79, 91, 115, 126, 85, 97, 70, 146, 103	1, 1, 1, 4, 1, 2, 2, 1, 3
10	31, 106, 156, 78, 179, 225, 240, 59, 188, 210	3, 1, 1, 1, 1, 1, 1, 1, 4, 2	174, 73, 166, 139, 120, 70, 85, 97, 154, 150	1, 2, 2, 1, 2, 3, 1, 1, 1, 1

linear arrray and all the multi-peak patterns contain peaks that are very narrow along with atleast one wide peak in the illumination pattern.

5.3.2 Properties of the Optimal Pattern

Qualitative Results

Table 5.4 shows the actual peak-positions and peak-widths for the two optimal three-peak illumination patterns. The illumination patterns are shown in Fig 5.6. The pattern has two narrow peaks and one wide peak in both test cases. This type of pattern helps move the first zeros in the DFT toward higher frequencies.

TABLE 5.4 Peak-positions and Peak-widths of Optimal Patterns

Number of Peaks	Test Case - I		Test Case - II	
	Peak - Positions	Peak - Widths	Peak - Positions	Peak - Widths
3	26, 212, 43	4, 1, 1	157, 177, 71	1, 4, 1

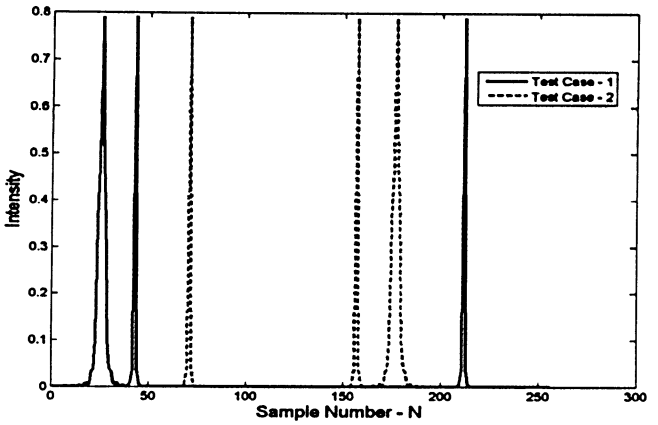

Figure 5.6 Three-peak illuminaiton pattern obtained from the test cases .

Fundamentally why is this pattern good? Some insight can be gained by looking at what happens with a 3-wide, and 3-narrow peak patterns. Some information regarding this behavior can be seen in Fig 5.7

Fig 5.7 shows the reciprocal of the magnitude of fourier transform of the pattern when all peaks are narrow($I_{narrow}[n]$). The sample numbers at which the magnitude are higher shows the existence of zeros in the DFT of the pattern. For a better understanding of this problem, it is good to re-cap the main components of linear-phase algorithm from Section 2.2.2.

Defining $S_0[n]$ as DFT of the zero shift signal and $S_\alpha[n]$ as the DFT of the shifted version, the exponential term can be isolated as follows:

$$Y[k] = \frac{S_\alpha[n]}{S_0[n]} = e^{-j\frac{2\pi k\alpha}{N}} \tag{5.2}$$

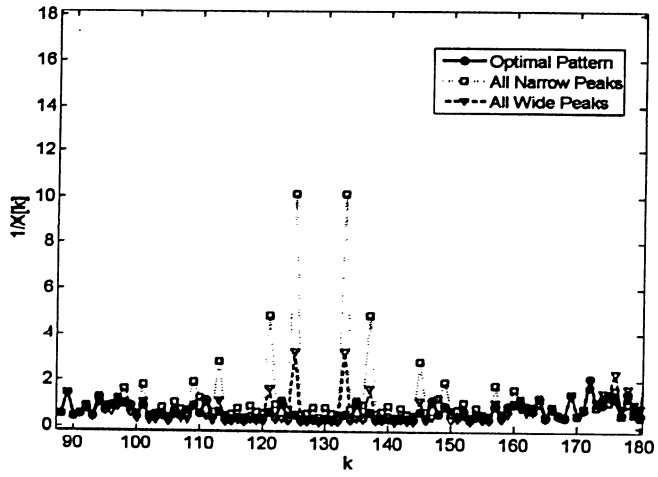

Figure 5.7 Fourier analysis of optimal, all narrow-peak, and all wide peak patterns.

If ψ is the phase angle of $Y[k]$, then it can be shown that:

$$\psi[k] = -\frac{2\pi k\alpha}{N} \tag{5.3}$$

The estimate of τ can be obtained from the calculated slope and the sample number n as follows: First, perform a least-squares fit using a sub-set of $\psi[k]$ to get an estimate $\tilde{\alpha}$ of the slope. An estimate of the displacement $\tilde{\tau}$ can then be calculated using:

$$\tilde{\tau} = \tilde{\alpha} \cdot \Delta X \tag{5.4}$$

To maintain good performance, the least-squares fit performed using a sub-set of $\psi[k]$ should be done carefully. The presence of zeros in the spectrum of $I_{narrow}[n]$ can cause severe distortions in the phase function. Samples in the centre (115-140) of the pixel array constitute the linear segment of the phase function using which the slope is calculated. The linear displacement of the shifted signal is estimated using this slope (Section 2.2.2). It can be observed from Fig 5.7 that, only the optimal pattern has distortions of low magnitude in the pixels that constitute the linear region of the phase function. In the case of all wide peaks and all narrow peaks in the pattern, the distortions are of higher magnitude which can affect the estimate of the linear shift in the pattern ($\tilde{\tau}$). Therefore, the optimal pattern was found to have

two narrow and one wider peak to help move the first zeros of the DFT towards higher frequencies.

Quantitative Results

This section examines the effect of increased noise on the performance of each super-resolution algorithm for the optimal illumination pattern. To justify the fabrication of the sensor's mask aperture, it is important to evaluate the performance of three-peak illumination pattern with other processing algorithms as a function of noise strength. The effective resolution values obtained from this simulation are shown in Fig 5.8.

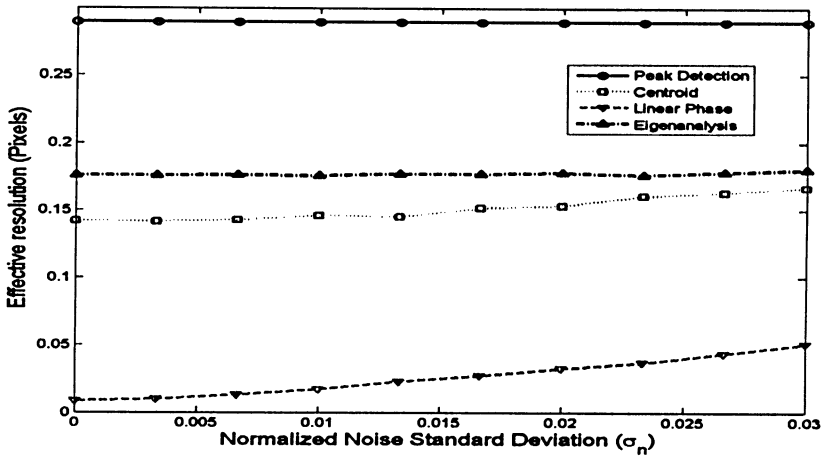

Figure 5.8 Variation of effective resolution with increasing noise for three-peak illumination pattern.

The effective peak-detection resolution remains constant throughout the test regime. This value is consistent with the observations made in Chapter 4. Since this algorithm uses a simple approach, it gains little from using additional peaks in the illumination pattern. Moving away from the peak location creates a sharp drop in the pixel illumination. Hence it becomes unlikely that increasing noise will cause the algorithm to mis-identify the peak.

The increase in effective resolution values for the centroiding algorithm can be attributed to the presence of two narrow peaks in the illumination pattern. For narrow peaks, the centroid

algorithms does not get enough samples to work with in the centroid window. This causes a bias in the estimate of τ. The performance of linear-phase algorithm is very encouraging. Although noise causes the performance of linear-phase algorithm to degrade, it displays better performance throughout the test regime when compared to other algorithms.

Eigenanalysis displayed the best results for most of the cases examined in Section 4.1. Therefore, the performance of eigenanalysis for the optimal pattern may be puzzling (Fig 5.8). Two important points to note are:

1. While optimizing the illumination pattern, the linear-phase algorithm was used to estimate the sun displacement. The optimizer produced a pattern that performed better only with the linear-phase algorithm. Therefore, the same pattern cannot be expected to perform well with eigenanalysis even though both the algorithms belong to the parametric algorithms category.
2. Eigenanalysis method had shown degradation in performance when compared to linear-phase algorithms in Section 4.2.2.

Since N2 pattern was considered as the best pattern among N1, W1, and W2, the relative advantage of using peak-detection, linear-phase and eigenanalysis for the optimal pattern against N2 pattern is examined in Fig 5.9. The linear-phase algorithm demonstrates gains of

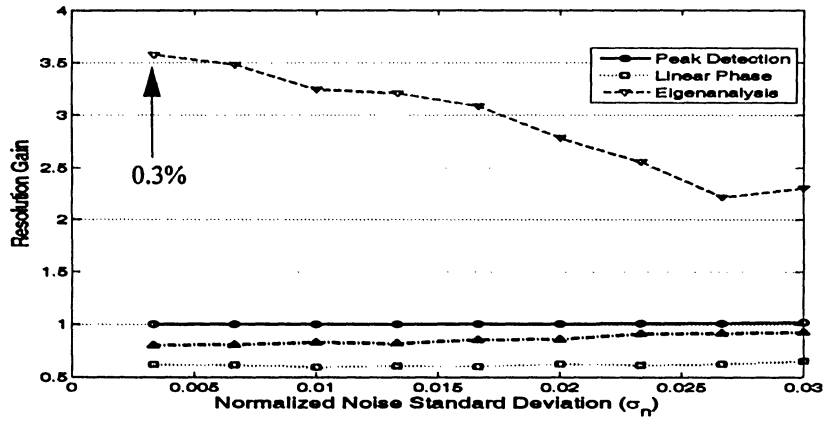

Figure 5.9 Effective resolution improvement relative to N2 pattern with increasing noise for three-peak illumination pattern.

more than 2 throughout the test regime, when compared to the performance of the other algorithms. Peak-detection, centroiding, and eigenanalysis display poor performance for the optimal pattern. This shows that, the pattern is only good with linear-phase algorithm.

5.3.3 Sensitivity Analysis

In order to examine the optimality of the GA solutions, the sensitivity of the optimized patterns, to changes in their chromosomes is investigated. Fig 5.10 shows the effect of varying the peak-width and peak-position on the system performance.

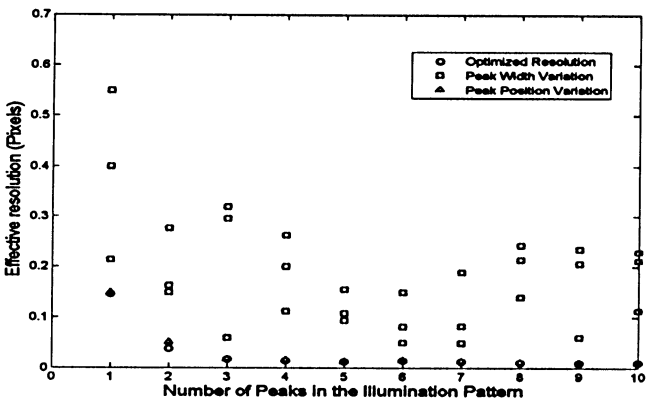

Figure 5.10 Effective resolution obtained from GA coupled with results from sensitivity analysis.

This was accomplished by dithering elements of the patterns' chromosomes. Separate tests were carried out for peak-widh variation, and changing peak-positions. Variations in peak-width from the optimal values cause considerable degradation in the system performance. Generally narrow peaks are preferred over wide peaks. This is consistent with the observations made in Section 4.2.1; wide peaks will have narrow transforms and hence the linear region of the phase function will shrink. In contrast, we see that varying the peak-position has little effect on system performance.

From Fig 5.10, the performance of the dithered patterns is nearly indistinguishable from the optimized patterns. In Fig 5.11, the variation in effective resolution values are visible clearly

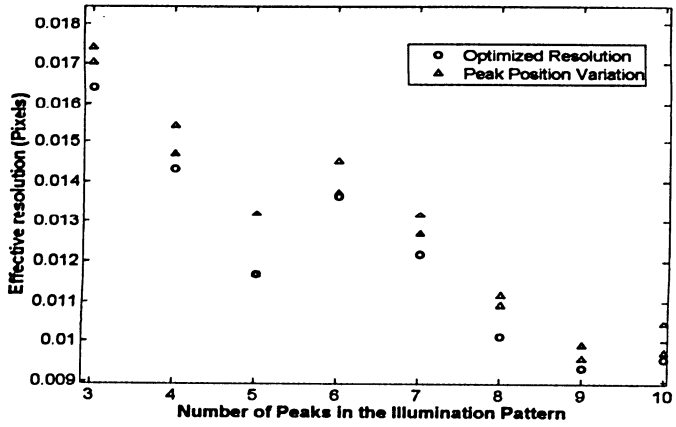

Figure 5.11 Detailed view of peak-position variation.

for peaks ranging from 3 to 10. The magnitude of the variation is less compared to the sensitiveness of peak-width to the optimal values. Therefore, the optimized illumination patterns are very sensitive to peak-widths, but fairly insensitive to peak-position.

5.4 Optimization Conclusion

This chapter provided a methodology for optimizing the sun-sensor illumination pattern using GAs. It was shown that simple changes to the illumination pattern of a digital sun-sensor can results in a three-fold increase in performance over the baseline two-slit sensor. A three slit illumination pattern was chosen as the most practical new pattern since it gave a good performance with the smallest change from the original pattern. Fabrication of such a optimized pattern is not expected to be difficult. The existing masks are laser etched and the revised pattern can be created using the same process. The required sun-sensor slits lie in the range of 10-30 μm with tolerances on the order of 1 μm. Redesigning the mask creates little if any cost impact to the sensor since the only change is the pattern etched in the front surface.

Chapter 6

IMAGE ARTEFACTS AND NOISE MODELS

Noise modelling is essential in any photometric endeavor. Several noise sources are typically considered when using pixel sensors. Image degradation due to different noise sources could have an effect on the performance of parametric algorithms that require a pre-defined model of the image. These sources can be divided into two types: *internal*, and *external* noise sources. Internal noise sources arise due to various components within the sensor. External sources include, effect of albedo from Earth, and other bodies in space.

In the simulations examined in Chapter 4, a simple noise model was used. The parametric algorithms displayed good performance with the simple noise model. This model only included an AWGN noise term. The inaccuracies introduced by using an enhanced noise model, by considering internal noise sources must also be evaluated to demonstrate its impact on the performance of the sun-sensor model used in this study. A realistic estimation of the noise-level would require a very sophisticated noise model. However, in this chapter an enhanced noise model is developed to evaluate the performance of the super-resolution algorithms.

Although many satellites are influenced by the Earth's albedo, few models of the effect exist. For sun-sensors onboard a satellite, Earth albedo is often treated as noise. Digital sun-sensors are mostly insensitive to albedo light [Hales & Pederson, 2001]. However, some configurations result in errors in the least significant bits of the digital sun-sensors [Brasoveanu & Sedlak, 1998]. This decreases the accuracy of these sensors when part of the

illuminated Earth surface is present in the sensor field-of-view. Therefore, this chapter will also evaluate the performance of super-resolution algorithms, when image artefacts due to Earth albedo are considered.

6.1 Component Noise Model

The detector array of the SS-256 sensor consists of 256 photodiodes, arranged in a linear array. Light energy impinging on a pixel generates photocurrent, which is then integrated by the circuitry associated with that pixel. The ideal response from each pixel is directly proportional to the light intensity on that pixel and the integration time. However, the actual image intensity from a pixel deviates from this ideal linear model. There are several independent sources of error that corrupt the photoelectronic transformation [Tsin et al, 2001].

This section presents a new model of noise for use in the syntesis of sensor images. Each *component* of the noise model represents a separate physical process. Three noise sources, namely *quantization error*, *shot noise*, and *Additive White Gaussian Noise* (AWGN) was considered in this component noise model.

6.1.1 Quantization Error

Quantization error is the noise error introduced by quantization in analog-to-digital conversion (ADC) process in the sensor system. If the value of the analog signal at a sample point falls between two quantization levels, the ADC treats it as if it were exactly one of the two values, thus introducing an error, known as quantization error. This is denoted by $w_q[n]$.

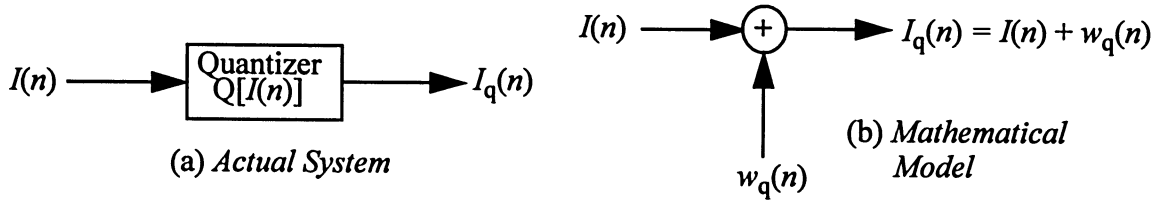

Figure 6.1 Mathematical model of Quantization Noise.

The mathematical model for the quantization error is shown in Fig 6.1. The maximum value of this error is half the value of the Least Significant Bit (LSB) of the ADC. This error is also referred to as quantization noise. The properties of $w_{quant}[n]$ are:

- The error $w_{quant}[n]$ is uniformly distributed over the range $-\frac{1}{2}LSB < w_{quant}[n] < \frac{1}{2}LSB$. In other words, the instantaneous quantizer error cannot exceed half of the quantization step. It is a zero mean random variable with a variance, $\sigma^2_{quant} = \frac{1}{12}LSB^2$ [Oppenheim & Schafer, 1975].
- The error $w_{quant}[n]$ and the error $w_{quant}[m]$ for $m \neq n$ are uncorrelated.
- The LSB for this model is taken as 1 count. Therefore,

$$-0.5 < w_{quant}[n] < 0.5 \tag{6.1}$$

Thus, for a m- bit ADC, $w_{quant}[n]$ is uniform over $\pm \frac{A}{2^{m+1}}$.

6.1.2 Shot Noise

Shot noise results from the inherent statistical variation, or uncertainty, in measuring the number of photons stored on each pixel of the detector array [Healey & Kondepudy, 1994]. The number of photons received is governed by Poisson's statistics, and is directly proportional to the integration time τ_{int}. Consider the arrival of photons over one such integration time τ_{int}. For a particular pixel, the mean rate of the Poisson process is the rate of electron arrival:

$$v_n = \frac{I(\tau_{int})}{e} \tag{6.2}$$

where e is the charge of the electron, and I represents a set of image data. The photon arrival times obey Poisson statistics and the number of photons, N_n, arriving within the integration time τ_{int} is a statistical variable determined by the Poisson distribution [McNeil et al, 2003]:

$$P(N_n) = \frac{\bar{N}_n^{N_n} e^{-\bar{N}_n}}{N_n!} \tag{6.3}$$

where $\bar{N}_n = v_n \tau_{int}$ is the expectation for the number of photons in the interval τ_{int}. Shot noise is a fundamental limitation and it cannot be eliminated. It is proportional to the integration time and the pixel intensity. Photoelectrons generated within the device constitute the signal whose amplitude will randomly fluctuate at each pixel. The shot noise $w_{shot}[n]$, for the sensor model used in this study can be modelled as a random variable that follows a Poisson distribution with mean and variance, $\sigma^2_{shot} = \bar{N}_n$.

6.1.3 Dark Current Noise

The *dark current noise* arises from statistical variation in the number of electrons thermally generated inside the silicon structure of the detector array. This small fluctuation can be modeled as Gaussian Noise. This can be included in the AWGN noise term of the component noise model. Another component of dark noise arises depending heavily on the device temperature, which often holds a constant d.c. offset added to the observed intensity [Barducci et al, 2005]. This can be compensated for during pre-processing.

6.1.4 Secondary Noise Sources

The noise sources discussed in this section can be compensated for during processing or calibration. One of these is the *fixed pattern noise*. Processing errors during the fabrication of the pixel array can cause small variations in quantum efficiency and charge collection volume from pixel-to-pixel [Debevec & Malik, 1997]. Therefore, if a pixel array is uniformly illuminated, these variations will lead to a pixel-to-pixel non-uniformity in collected charge. This phenomenon is called the fixed pattern noise (FPN). Therefore, (FPN) is basically a distortion of the image due to variations in device parameters across the sensor. This can be modeled by a constant multiplier associated with each pixel in the detector array. FPN can be corrected for by calibrating each pixel individually. This calibration is obtained by taking a large number of images using a uniform illumination and calculating the ratio of the mean count over the whole sensitive area to the accumulated count of the individual pixel [Tlustos et al, 2003] Amplifier noise can be modeled as AWGN term.

6.1.5 Model Synthesis

The noise sources discussed in the previous sections form the component noise model for this study. The standard deviation of the component noise model is as shown below:

$$\sigma_{total} = [\langle\sigma^2_{shot}\rangle + \langle\sigma^2_{quant}\rangle + \langle\sigma^2_{AWGN}\rangle]^{1/2} \tag{6.4}$$

The AWGN term now contains a number of residual effects (Dark current, amplifier noise, etc.). The amplitude of this noise model is normalized to the maximum intensity value in the illumination pattern.

6.2 Performance Analysis of Component Noise Model

The performance of super-resolution algorithms as a function of noise strength for different illumination patterns were discussed in Chapter 4. The sensor model only included an AWGN term. The component noise model derived in Section 6.1 was tested with three different illumination patterns. (a) Narrow, single-peak image (baseline pattern, N1), (b) Narrow, two-peak image (N2), and (c) Optimized illumination pattern.

Fig 6.2 shows the ratio of δ_{eff} values of the component noise model to the simple noise model for all the three candidate illumination patterns. The ratio is computed as follows:

$$Gain = \frac{\delta_{eff,AWGN}}{\delta_{eff,component}} \tag{6.5}$$

- All three candidate illumination patterns display similar (approximately) resolution gains. The effective resolution values for N1, N2, and the optimal pattern, obtained by using a component noise model, with respect to a simple AWGN term were found to be the same. Therefore, the ratio is close to unity.
- Thus, the inaccuracy introduced by using a component noise model rather than a single AWGN term was judged to be negligible.

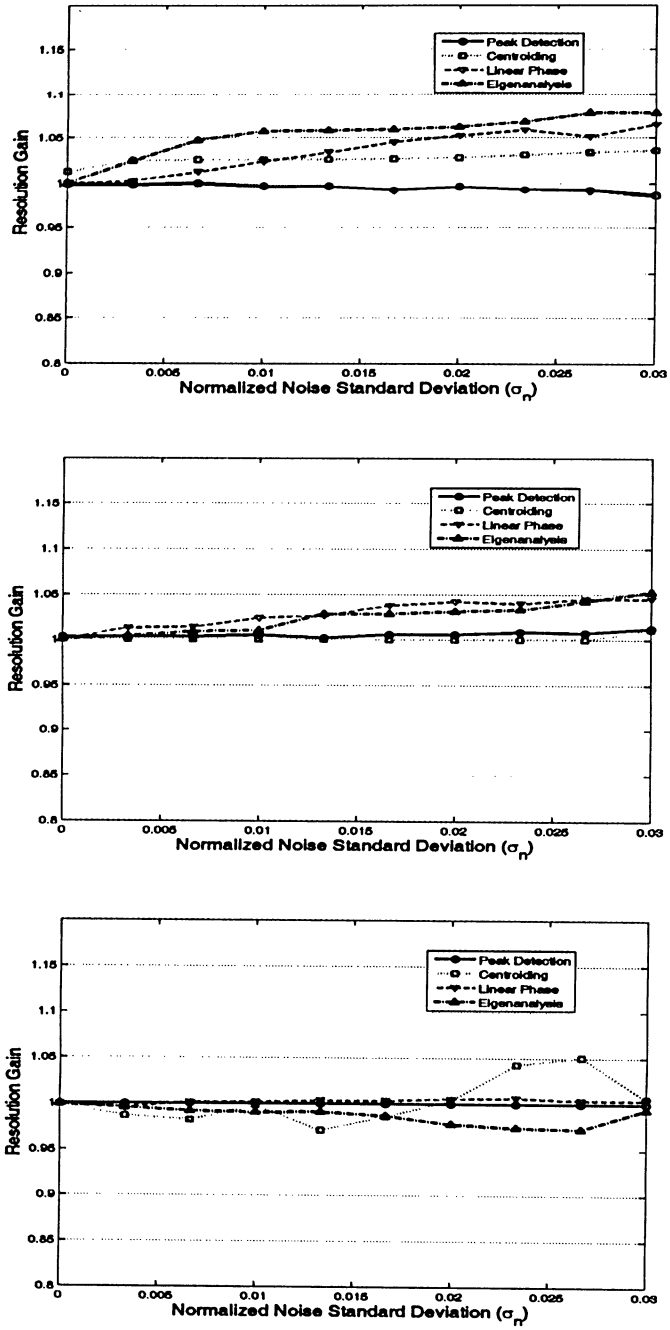

Figure 6.2 Comparison of effective resolution values for N1, N2, and optimal illumination patterns, tested with Component noise model and only the AWGN term.

6.3 Earth Albedo Modeling

All sun-sensors are designed based on the assumption that there is only one bright object i.e. the Sun, is present within the sensor field-of-view. Existing sun-sensors cannot distinguish the effect of a single light source if sever bright objects are simultaneously visible. Therefore, Earth Albedo interference will degrade the accuracy of sun-sensors. An analysis of Solar Maximum Mission flight data showed that *fine sun-sensor* measurements were affected by Earth albedo [Ryer, 1997]. A subsequent study based on a detailed theoretical model of Earth albedo effect on *coarse sun-sensors*, *digital sun-sensors*, and *fine sun-sensors* shows that accuracy of all types of sun-sensors degrade adversely [Brasoveanu et al, 1990]. The degradation is based on spacecraft, Earth and Sun positions, sensor boresight orientation, and sensor design data. Most of the time digital sun-senors are not affected, but for brief periods of time the Earth albedo can cause errors which may exceed one degree.

The main objective of this study is to evaluate some questions that are related to albedo effect on digital sun-sensors.

- Is the accuracy of digital sun-sensors reduced by the effect of Earth albedo interference?
- Is it possible to model and accurately analyze the effect of illuminated Earth on digital sun-sensor measurements?

6.3.1 Reflectivity Data

To get a realistic reflectivity distribution, reflectivity data from existing measurements is analyzed. The modeling of Earth albedo is based on the reflectivity data, measured by the Earth Probe Satellite of the Total Ozone Mapping Spectrometer (TOMS) [Ryer, 1997]. The satellite data are given in a resolution of $\Delta\phi_g = 1$ deg latitude times $\Delta\theta_g = 1.25$ deg longitude, i.e. 180 x 288 data points. Fig 6.3 shows the Earth surface divided into a set of area elements using a map-like grid.

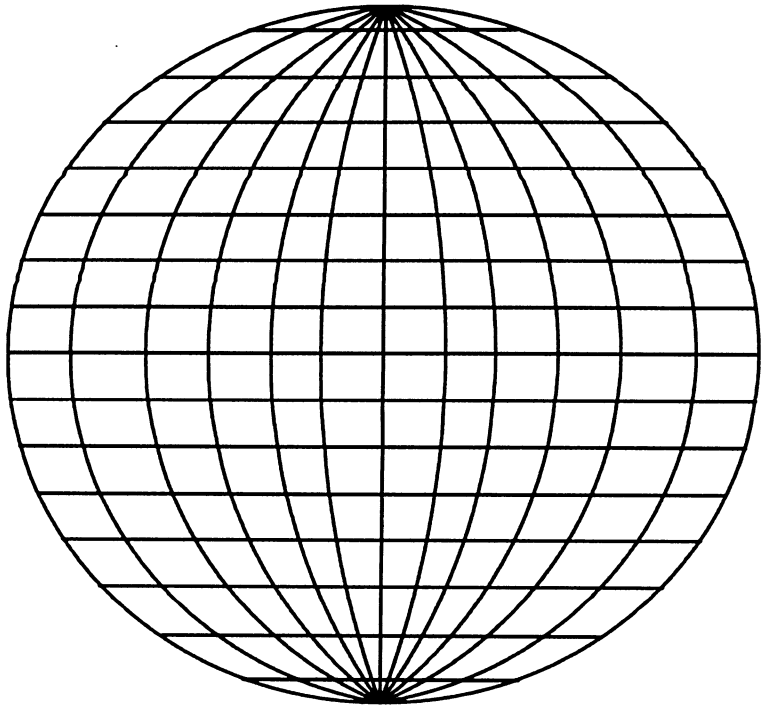

Figure 6.3 Earth surface grid of elements.

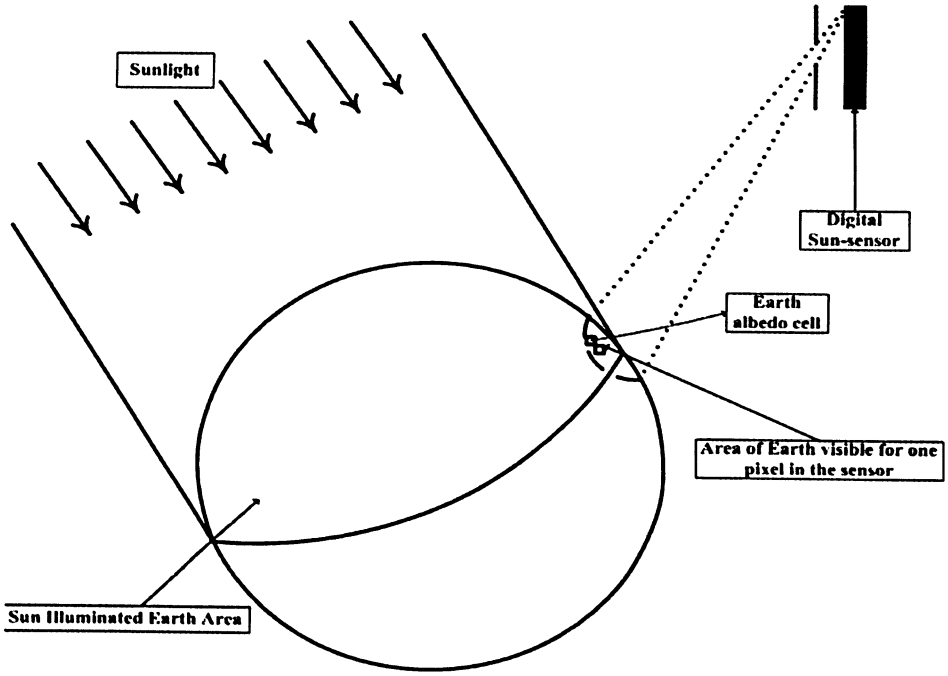

Figure 6.4 Sun-sensor, Earth, and Sun geometry.

The two dimensional data space $\boldsymbol{D}$ is defined as a grid of data points Φ x Θ, where

$$\begin{aligned} \Phi &= \{0, \Delta\phi_g, 2\Delta\phi_g, \ldots, 179\Delta\phi_g\} \\ \Theta &= \{0, \Delta\theta_g, 2\Delta\theta_g, \ldots, 287\Delta\theta_g\} \end{aligned} \tag{6.6}$$

To each data point $(\phi_g, \theta_g) \in D$, the mean reflectance of a cell, $\phi_g \pm \frac{\Delta\phi_g}{2}$ and $\theta_g \pm \frac{\Delta\theta_g}{2}$, on the Earth surface is available in the TOMS data product.

6.3.2 Reflection of Incident Irradiance

The modeling approach used in the section has been adapted from [Bhanderi & Bak, 2005]. The authors use the TOMS reflectivity data to derive the reflection of incident irradiance from the Earth surface. The amount of albedo incident on the sun-sensor will be discussed in the next section. The incident solar irradiance hits a cell on the surface of the Earth at a grid point (ϕ_g, θ_g), at an incident angle of α_{sun} to the cell normal $\hat{n}_c$. It is modeled as a black body source, and the total irradiance is the sum of the irradiances in the black body spectrum. The irradiance[1] is found to be $E_{AMO} = 1367 W/m^2$.

The amount of radiant flux reflected by a cell, at grid point $(\phi_g, \theta_g) \in D$, depends on irradiance and the area of the cell, $A_c(\phi_g)$. Given the angle of the grid center ϕ_g, the grid area is given by (6.7), where r_E is the Earth mean radius.

$$A_c(\phi_g) = \theta_g r_E^2 \times \left\{ \cos\left(\phi_g - \frac{\Delta\phi_g}{2}\right) - \cos\left(\phi_g + \frac{\Delta\phi_g}{2}\right) \right\} \tag{6.7}$$

The incident irradiance on the cell is equal to the solar AMO irradiance multiplied by a cosine term dependant on the incident angle α_{Sun}, which is the angle between the cell normal $\hat{n}_c$ and the Sun line-of-sight (LOS) vector from the grid point, $\hat{r}_{Sun}$. The intensity of the incoming irradiance decreases as the angle of incidence increases. This is equivalent to the observed call

1. The subscript AMO states that the irridiance has passed through zero air mass.

area as seen from the Sun. The incident radiant flux density $P_c(\phi_g,\theta_g)$ on a single cell at grid point (ϕ_g,θ_g), is given by

$$P_c(\phi_g,\theta_g) = E_{AMO}A_c(\phi_g)\{\hat{r}_{Sun}^T\hat{n}_c\}\Big|_0^8 \tag{6.8}$$

Note that the vectors $\hat{r}_{Sun}$ and $\hat{n}_c$ are functions of data grid point (ϕ_g,θ_g). The reflection on the Earth surface is assumed to be Lambertian [Ryer, 1997]. The reflected radiant flux density $P_r(\phi_g,\theta_g)$, also known as radiant exitance, is calculated as a fraction $\rho(\phi_g,\theta_g)$ of the incoming radiant flux in (6.8)

$$P_r(\phi_g,\theta_g) = \rho(\phi_g,\theta_g)P_c(\phi_g,\theta_g) \tag{6.9}$$

where $\rho(\phi_g,\theta_g)$ is the mean reflectivity at grid point $(\phi_g,\theta_g) \in D$. The irradiance $E_r(\phi_g,\theta_g)$ of the cell, when assuming Lambertian reflectivity is related to the radiant exitence [Ryer, 1997] by

$$E_r(\phi_g,\theta_g) = \frac{P_r(\phi_g,\theta_g)}{\pi} \tag{6.10}$$

The Inverse Square Law states that the intensity of the irradiance decreases with the square of the distance from the grid point to the sun-sensor, which can be written as

$$E_{ss}(\phi_g,\theta_g) = \frac{E_r(\phi_g,\theta_g)}{\|\hat{r}_{ss}\|^2} \tag{6.11}$$

where $\hat{r}_{ss}$ is the sun-sensor LOS vector. Finally, the irradiance at each pixel on the detector array of the sensor, depends on the visible area of the cell surface seen from the sun-sensor. This will be discussed in detail in the following section.

6.3.3 Earth Albedo at Sun-sensor

The single-slit sun-sensor model was used to evaluate the performance of sensor processing techniques under the influence of Earth albedo. The amount of Earth albedo from a single cell, seen for each pixel in the sun-sensor can be estimated using 3-D Ray Tracing. Each cell can contribute albedo to more than one pixel in the detector array.

Fig 6.5 shows a detailed schematic of the ray tracing procedure adapted in this section. Rays from an albedo cell c_{ij}, passes through one edge of the slit and hits a particular location on the detector array. Another ray can also pass through the second edge of the slit and hit the detector array at a different pixel. Therefore, all the pixels between the first and the second hit locations will receive Earth albedo from that particular cell c_{ij}.

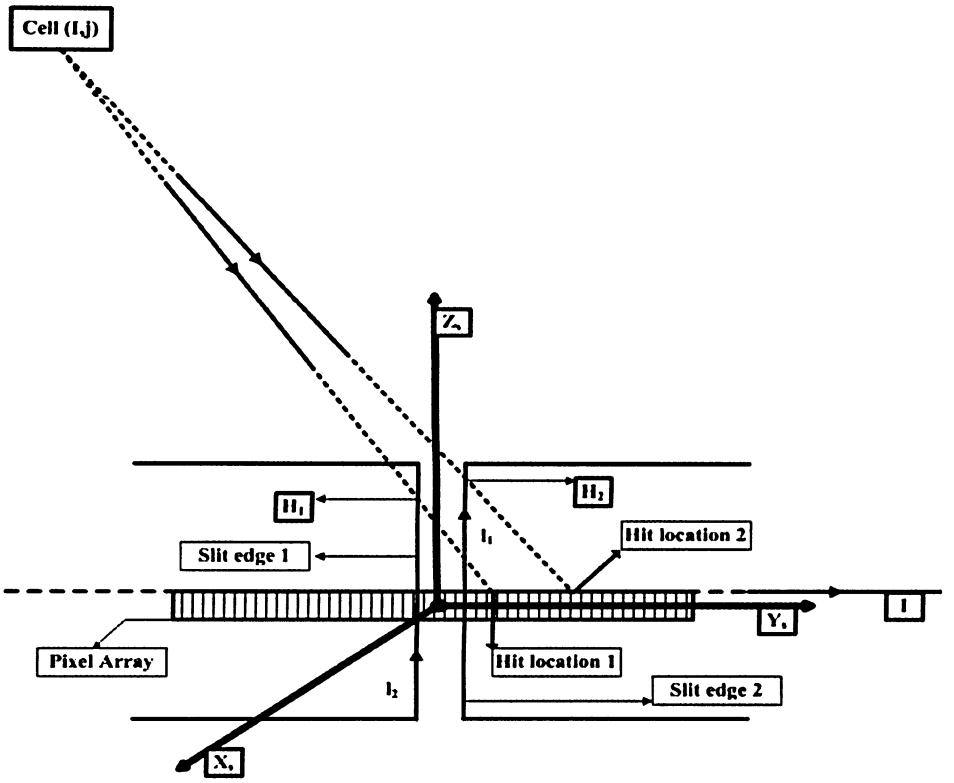

Figure 6.5 Ray tracing from each albedo cell on Earth to the sun-sensor's detector array.

The detector is a 256 pixels linear array, and (X_{ss},Y_{ss},Z_{ss}) defines the sensor reference frame whose origin lies at the centre of the detector. Y_{ss}-axis is along the linear pixel array.

In Fig 6.5, $\vec{l}$ is the line along the pixel array. $\vec{l}_1$ and $\vec{l}_2$ are lines defining the two edges of the slit. If $\vec{V}_o$ is the position vector of cell c_{ij} in the sensor reference frame and, $\vec{V}_1$ and $\vec{V}_2$ are any two points on line $\vec{l}$, then $\vec{V}_o$, $\vec{V}_1$, and $\vec{V}_2$ can be considered as the three points which constitute the plane of the ray from cell c_{ij} to the linear pixel array.

The lines defining the two edges of the slit can be written as

$$\begin{aligned} \vec{l}_1 &= \vec{l}_{A1} + a(\vec{l}_{B1} - \vec{l}_{A1}) \\ \vec{l}_2 &= \vec{l}_{A2} + a(\vec{l}_{B2} - \vec{l}_{A2}) \end{aligned} \tag{6.12}$$

where $\vec{l}_{A1}$, $\vec{l}_{B1}$, are two points in the line $\vec{l}_1$, and $\vec{l}_{A2}$, $\vec{l}_{B2}$ are two points in the line $\vec{l}_2$. They are defined as:

$$\begin{aligned} \vec{l}_{A1} &= \begin{bmatrix} h \\ -w \\ 1 \end{bmatrix} \qquad \vec{l}_{B1} = \begin{bmatrix} h \\ -w \\ 2 \end{bmatrix} \\ \vec{l}_{A2} &= \begin{bmatrix} h \\ w \\ 1 \end{bmatrix} \qquad \vec{l}_{B2} = \begin{bmatrix} h \\ w \\ 2 \end{bmatrix} \end{aligned} \tag{6.13}$$

where h is the vertical distance from the pixel array to the slit along the x-axis, and w is the half-width of the slit. Considering $\vec{H}_1$ as the point of intersection of the first ray on one edge of the slit $\vec{l}_1$, then:

$$\vec{H}_1 = \vec{l}_{A1} + a^*(\vec{l}_{B1} - \vec{l}_{A1}) \tag{6.14}$$

where $a^* = \dfrac{\hat{n} \bullet (\vec{V}_0 - \vec{l}_{A1})}{\hat{n} \bullet (\vec{l}_{B1} - \vec{l}_{A1})}$ and the normal, $\hat{n}$ of the plane of the ray is given by:

$$\hat{n} = (\vec{V}_2 - \vec{V}_0) \times (\vec{V}_1 - \vec{V}_0) \tag{6.15}$$

The line of the pixel array can be defined as

$$\vec{l} = \vec{V}_2 + t^*(\vec{V}_1 - \vec{V}_2) \tag{6.16}$$

The ray originating from $\vec{V}_o$ strikes a point l^* on line $\vec{l}$, after it passes through $\vec{H}_1$. This hit location can be calculated as follows:

$$\vec{V}_0 + S(\vec{H}_1 - \vec{V}_0) = \vec{V}_2 + t^*(\vec{V}_1 - \vec{V}_2) \tag{6.17}$$

Finding the value of t^* and substituting that in (6.16) gives the hit location of the ray originating from $\vec{V}_o$ and passing through one edge of the slit at $\vec{H}_1$. The second hit location on $\vec{I}$, can be calculated in a similar manner for the ray that passes through the other edge of the slit at $\vec{H}_2$.

The hit locations are converted to pixel numbers, that represent the hit points, within the pixel array. After performing this calculation for the entire set of cells that are in the field-of-view of the sun-sensor, the total albedo on each pixel in the array is calculated by summing the albedo effect of several cells on each pixel. If a_{ij} is the albedo contribution of cell C_{ij}, then the total albedo A_k on a pixel k can be shown as:

$$A_k = \sum a_{ij} \qquad \forall i,j \tag{6.18}$$

Due to low resolution of data sets, the final albedo does not form a good profile. A little hand tuning is required to interpolate between few pixel numbers to obtain a good shape of the image of the Earth's albedo.

6.4 Earth Albedo Performance Analysis

In this section, the results of Earth Albedo model are presented. The effect of Earth albedo on the performance of super-resolution algorithms in estimating the sun-angle, is examined by considering two test cases that describe different combinations of the sun-sensor orientation, Earth, and the Sun geometry. Fig 6.6 shows a schematic representation of the test cases.

The two specific combinations that were examined are:

- Case (I) - The sun-sensor receives full illumination of the Earth albedo and the sun-position is varied by rotating the sensor about its boresight (Fig 6.6.(I)). Three sub cases considered are: (i) Sun-peak perfectly overlapping the broad Earth albedo, (ii) Sun-peak at the extreme left of the pixel array, and (iii) Sun-peak at the extreme right of the pixel array.

- Case (II) - In this test case, the sensor pixel array receives only partial illumination of the Earth albedo (Fig 6.6(II)). This can be attained if the spacecraft is in a different position in its orbit, away from the full Sun-lit Earth field-of-view. Thus, the sensor will be exposed only to a part of the Earth albedo. This was tested with varying Sun-peak positions explained in Case (I).

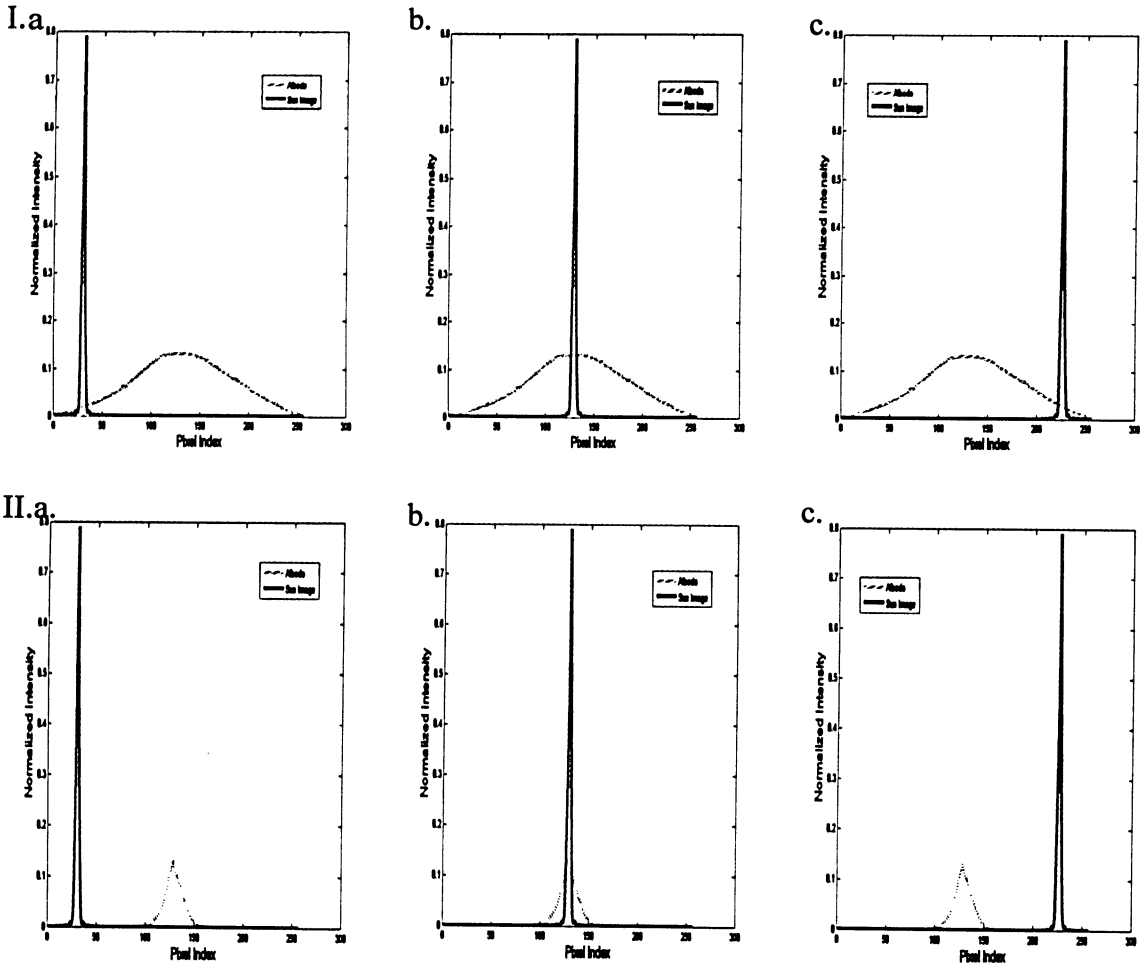

Figure 6.6 Sample image at the pixel array. Case (I) represents Sun-images with full illumination of Earth, Case(II) Sun-images with partial Earth Albedo, Case(III) Partial overlap of Sun Image with Earth Albedo.

The results for all the six cases above are shown below in Table 6.1 to Table 6.4. tablettt

TABLE 6.1 Effect of Earth albedo for Peak-detection Algorithm

Case	δ_{eff} no albedo	δ_{eff} albedo	Ratio
I a	0.2896	0.2895	1
I b	0.2895	0.2895	1
I c	0.2895	0.2895	1
II a	0.2896	0.2896	1
II b	0.2895	0.2895	1
II c	0.2895	0.2895	1

TABLE 6.2 Effect of Earth albedo for Centroiding Algorithm

Case	δ_{eff} no albedo	δ_{eff} albedo	Ratio
I a	0.0142	0.028	0.51
I b	0.0146	0.1181	0.12
I c	0.0146	0.0394	0.37
II a	0.0142	0.0142	1
II b	0.0146	0.1008	0.14
II c	0.0146	0.0146	1

TABLE 6.3 Effect of Earth albedo for Linear-phase Algorithm

Case	δ_{eff} no albedo	δ_{eff} albedo	Ratio
I a	0.0067	0.0067	1
I b	0.0071	0.0071	1
I c	0.0066	0.0066	1
II a	0.0067	0.0068	1
II b	0.0071	0.0093	0.76
II c	0.0066	0.0066	1

TABLE 6.4 Effect of Earth albedo for EigenanalysisAlgorithm

Case	δ_{eff} no albedo	δ_{eff} albedo	Ratio
I a	0.0096	0.0093	1.03
I b	0.0095	0.0077	1.23
I c	0.0093	0.0087	1.07
II a	0.0096	0.0096	1
II b	0.0095	0.0231	0.4
II c	0.0093	0.0093	1

The following observations can be made from Table 6.1 to Table 6.4:

- Peak detection algorithm performs invariantly with and without the presence of Earth albedo.
- Centroiding algorithm displays poor performance when the sun-peak fully overlaps the albedo pattern (Case - I b & II b) for both full and partial illumination of the Earth albedo.
- Linear-phase algorithm performs well with full illumination of the Earth albedo (Case I - a,b,c). For Case II b, when sun-peak fully overlaps the narrow albedo pattern, this algorithm shows a small degradation in performance.
- Eigenanalysis demonstrate excellent performance in the presence of full illumination of Earth albedo (Case I, a,b,c). For Case II b, it displays bad performance with overlap of sun-peak and narrow pattern
- Looking at just the δ_{eff} values, in the presence of Earth albedo, linear-phase algorithm performs better than any other algirthm under consideration in this test.
- Parametric methods continue to perform better than the conventional 'smart' approach - centroing.

6.5 Summary

This chapter introduced advanced noise modeling to examine the performance of super-resolution algorithms in estimating the sun-angle. A component noise model that included quantization error, shot noise, and the AWGN term was developed and tested with different sun-sensor illumination patterns. The results showed that adding a component noise model to the calculations made little impact on the performance of super-resolution algorithms for all the tested illumination patterns. The difference between the performance of super-resolution algorithms using a component noise model when compared to using only an AWGN term was found to be negligible.

The effects of Earth albedo in modifying the incoming illumination pattern on the detector array was analyzed. After modeling the Earth albedo based on [Bhanderi & Bak, 2005], the amount of albedo seen by each pixel in the array was calculated using a simple ray tracing method. The resulting albedo pattern along with a Sun illumination pattern at different positions on the pixel array, were tested for algorithmic performance. Parametric algorithms displayed good performance throughout the test regime. There was little effect on the accuracy of the sensor-model when Earth albedo was tested with parametric algorithms. Linear-phase algorithm yielded sizeable improvements in sun-displacement estimates when compared to the conventional centroiding algorithm. Thus, parametric algorithms demonstrate immunity to albedo interference.

Chapter 7

CONCLUSIONS

The goal of this study, as outlined in Chapter 1, was to examine several approaches that could improve the angular accuracy of digital sun-sensors. The main focus was on developing super-resolution algorithms that can provide subpixel accuracy in estimating the sun illumination displacement. Using these algorithms, other re-design strategies were evaluated.

7.1 Summary

This section provides an outline of key features and other results observed in the previous chapters.

7.1.1 Background

Detailed analysis of various centroiding algorithms used in Star sensors were investigated. It was established that certain centering algorithms when slightly modified to suppress the sky background below a prechosen threshold level can significantly improve the accuracy of star image processing. Advantages and disadvantages of each of the methods were examined.

Parametric algorithms play a vital role in estimation of lateral shift in two similar images. The theoretical background of phase-correlation method was introduced in this section. It was shown that, this method can also be used in signal analysis. The linear-phase algorithm later derived in Chapter 3 was based on the fourier shift property of this method. MUSIC algorithm is used widely for time delay estimation in many application. If combined with other methods,

then MUSIC can be used to estimate various parameters related to a signal. The eigenanalysis algorithm examined in Chapter 3 was one of derivatives of MUSIC algorithm.

7.1.2 Design Evaluation Framework

A fairly representative of modern sensors made by Sinclair Interplanetary was used to describe the characteristic parameters of the sensor model. The analytical sensor model was used to determine the illumination pattern. Noise in the model were introduced by using a single AGWN term.

Theoretical framework of super-resolution algorithms used in this study were developed. Four algorithms were evaluated: two were conventional algorithms common to spacecraft sensors (Peak-detection, Centroiding); two were parametric algorithms employed in other fields of signal processing. To quantitatively assess the results of the simulations, a performance metric called the *effective resolution* δ_{eff} was derived. Another metric called the *performance gain, G* was also introduced to compare algorithms, illumination patterns, and noise levels or some combination of the above.

'Smarter' sun-sensor algorithms come at the cost of additional processing requirements. Table 2 presents a qualitative comparison of the mathematical operations required for each algorithm and their overall computational costs. Assessing the attractiveness of any new technique, entails weighting the potential improvement in performance and the cost of adopting the new technology.

The conventional techniques, peak-detection and centroiding, are computationally simple. This is consistent with their continuing popularity in many classes of spacecraft. The parametric methods require substantially more processing than conventional algorithms. Moreover, there is a large computational difference between linear phase and eigenanalysis methods.

TABLE 7.1 Comparison of algorithm requirements

Algorithm	Required Mathematical Operations	Computational Requirements
Peak-detection	Maximization	Very Low
Centroiding	Weighted sums	Low
Linear-phase	DFT, Least Squares line fit	Medium
Eigenanalysis	DFT, Cross-correlation, Iterative Minimization, Eigen Value Decomposition (EVD)	High

7.1.3 Performance Evaluation

The algorithms were tested using different procedures. The effects of system noise on algorithm performance was first examined for a baseline pattern, and then other simple patterns were tested. It was shown that under low-noise operational conditions, linear-phase and eigenanalysis algorithms yielded sizeable improvements in sun displacement estimates. Presently it is not clear that these improvements are dramatic enough to justify the added computational load that these methods require. However, the gains from parametric algorithms when compared the standard centroiding algorithm are encouraging enough to validate this approach worthy of future study. These improvements were demonstrated in simulation and supported by experimental validation [Enright & Godard, 2005].

Multi-peak patterns were found to be a highly desirable modification. Narrow peak patterns demonstrated better performance when compared to wide peak patterns. Thus, a general direction to look for 'optimal' illumination patterns was established.

7.1.4 Mask Optimization

In this section, it was shown that simple changes to the illumination pattern of a digital sun-sensor can result in a three-fold increase in performance over the baseline two-slit sensor. The results proved that patterns with multiple, narrow peaks provide sub-pixel accuracy in resolving the sun-angle. A three-slit pattern was chosen as the most practical new pattern since it gave a good performance with the smallest change from the original pattern.

Fabrication of such an optimized pattern is not expected to be difficult. The existing masks are laser etched and the revised pattern can be created using the same process. Therefore, redesigning the masks creates little, if any, cost impact to the sensor since the only change is the pattern etched in the front surface.

7.1.5 Image Artefacts and Noise Model

A component noise model was developed to evaluate the effect of other noise sources present when dealing with detector arrays. A model that includes shot noise, quantization error, and AWGN was derived. It was shown that, there was no change in performance of the algorithms when compared to the simulations done using just an AWGN term in the noise model. Therefore, the inaccuracies introduced using a single AWGN noise term rather than component noise model was found to be negligible.

The effects of image artefacts like Earth albedo was analyzed. An Earth albedo model based on TOMS reflectivity data and the work of [Bhanderi & Bak, 2005], was derived. The directional information of Earth albedo contribution from each cell was examined by using a ray tracing method. The amount of albedo on each pixel of the detector array was calculated. Using the albedo pattern on the pixel array, different geometries of spacecraft-earth-sun were examined. These geometries were tested for algorithm performance. Parametric algorithms continued to demonstrate excellent performance when compared to other methods. The linear-phase algorithm performed the best when compared to peak-detection, centroiding, and eigenanalysis.

7.2 Future Work

7.2.1 Improved Fidelity Sensor Models

The sensor model employed in this study is simple but crude. An improved model of the image-forming will give credence to the study results. Suggested improvements include:

- Two dimensional, non-paraxial diffraction propagation with extended sources.

- An expanded noise model that includes other noise sources like amplifier noise, reset noise, read noise, etc.
- Performance in the presence of image artefacts like dark/bright pixels.
- A model of component tolerances and calibration parameters.

7.2.2 Experimental Validation and Prototyping

Experimental validation is crucial for any new space technology. Not only must any new algorithm be tested in the laboratory for robustness and effectiveness, the implementation must also be optimized for deployment as flight software. To support the initial findings of laboratory experiment, the parametric algorithms must be subjected to more comprehensive, wide angle validation and the implementation of those algorithms should be prototyped in flight-like hardware.

7.3 Concluding Remarks

The parametric algorithms demonstrated excellent performance in all the test cases when compared with conventional processing techniques. The testing of component noise models and image artefacts further proved the consistency of the performance of parametric methods. The mask aperture pattern was optimized and a three-peak pattern looks to be promising. The Overall, the re-design goals set in the initial stages of the study was successfully validated.

REFERENCES

[Appel, 2003] Appel, P.; *Attitude Estimation from Magnetometer and Earth-Albedo Cor rected Coarse Sun Sensor Measurements*, 4th IAA Symposium on Small Satellites for Earth Observation, April 2003.

[Auer & van Altena, 1978] Auer, L.H.; van Altena, W.F.; Digital Image Centering. II, Astronomical Journal, Vol. 83, pg. 531-537, May 1978.

[Back et al, 1997] Back, T.; Fogel, D.B.; Michalewicz, Z.; *Handbook of Evolutionary Computation*, IOP Publishing, 1997.

[Barducci et al, 2005] Barduci, A.; Guzzi, D.; Marcoinni, P.; Pippi, I.; *CHRIS-Proba Performance Evaluation: Signal-to-Noise Ratio, Instrument Efficiency and Data Quality from Acquisitions over San Rossore Test Site*, Proc. of the 3rd ESA CHRIS/ Proba Workshop, March 2005.

[Bhanderi & Bak, 2005] Bhanderi, D.D.V.; Bak, T.; *Modeling Earth Albedo for Satellites in Earth Orbit*, AIAA Guidance, Navigation, and Control Conference, Vol.8, pg. 6220-6231, August 2005.

[Brasoveanu et al, 1990] Brasoveanu, D.; Aranshahi, H.; Phenneger, M.; *Study of Earth Albedo Interference on Sun Sensors*, Computer Sciences Corporation, CSC/TM-90/ 6103, September 1990.

[Brasoveanu & Sedlak, 1998] Brasoveanu, D.; Sedlak, J.; *Analysis of Earth Albedo Effect on Sun Sensor Measurements Based on Theoretical Model and Mission Experience*, AAS/GSFC 13th International Symposium on Space Flight Dynamics, Vol. 1, pg. 435-447, May 1998.

[Chen & Lerner, 1978] Wertz, J.; Chen, L.; Lerner, G.; *Sun Sensor Models - Spacecraft Attitude Determination and Control*, Kluwer, 1978.

[Chui, 1977] Chui, L.-T.G.; Astronomical Journal, 82, 842.

[Chui et al, 1979] Chui, L.,-T,G.; van Altena, W.F.; Stetson, P.B.; *International Workshop on Image Processing in Astronomy*, Proc. of the 5th Colloquium on Astrophysics, pg. 240-244, 1979.

[Coldrick, 1972] Coldrick, J.R.; *Optical Sensors for Spacecraft Attitude Determination, Optics and Laser Technology* , Vol. 4, No. 3, pg. 129-141, 1972.

[Debevec & Malik, 1997] Debevec, P.E.; Malik, J.; *Recovering High Dynamic Range Radiance Maps from Photographs*, In SIGRAPH'97

[Eid et al, 2001] Eid, E.; Chan, T.; Fossum, E.; Tsai, R.; Spagnuolo, R.; Deily, J.; Byers, W.; Peden, J.; *Design and Characterization of Ionizing Radiation-Tolerant CMOS APS Image Sensors upto 30Mrd (Si) Total Dose*, IEEE Transactions on Nuclear Science, Vol.48, No.6, Dec.2001.

[Enright & Godard, 2005] Enright, J.P.; Godard; *Super-resolution Techniques for Sun-Sensor Processing*, Submitted to IEEE Transactions on Aerospace Systems, Submitted August 2005.

[Falbel & Paluszek, 2001] Falbel, G.; Paluszek, M.; *An Ultra Low Weight/Low Cost Three Axis Attitude Readout System for Nano-satellites*, Proc. of IEEE Aerospace Conference, Vol. 5, pg. 2469-2481, March 2001.

[Farrell et al, 1995] Farrell, W.M.; Thompson, R.F.; Lepping, R.P.; Byrnes, J.B.; *A Method of Calibrating Magnetometers on a Spinning Spacecraft*, IEEE Transactions on Magnetics, Vol. 31, No.2, pg. 966-972, March 1995.

[Foroosh & Zerubia, 2002] Foroosh, H.; Zerubia, J.B.; *Extension of Phase-correlation to Subpixel Registration*, IEEE Transactions on Image Processing, Vol. 11, No. 3, pg. 188-200, March 2002.

[Fortescue, et al 2003] Fortescue, P.; Stark, J.; Swinerd, G.; *Spacecraft Systems Engineering*, Third Edition, John Wiley & Sons Ltd., 2003.

[Ge et al, 2004] Ge, F.; Shen, D.; Peng, Y.; Li, V.; *Super-resolution TDOA Estimation Based on Eigenanalysis and Sequential Quadratic Programming,* IEE Proc. - Radar, Sonar, and Navigation, Vol. 151, No. 4, August 2004.

[Goldberg, 1989] Goldberg, D.E.; *Genetic Algorithms in Search, Optimization, and Machine Learning*, Addisson Wesley Publishing Company, 1989.

[Goodman, 1996] Goodman, J.; *Introduction to Fourier Optics*, 2nd Edition, McGraw-Hill, 1996.

[Hales & Pederson, 2001] Hales, J.H.; Pederson, M.; *Two-axis MOEMS Sun Sensor for Pico Satellites,* 16th Annual AIAA/USU Conference on Small Satellites, 2001.

[Healey & Kondepudy, 1994] Healey, G.E.; Kondepudy, R.; *Radiometric CCD Camera Calibration and Noise Estimation*, IEEE Transaction on Pattern Recognition and Machine Intelligence, Vol.16, No.3, March 1994.

[Hoge, 2003] Hoge, W.S.; *A Subspace Identification Extension to the Phase-correlation*

Method, IEEE Transactions on Medical Imaging, Vol. 22, No. 2, pg. 277-280, February 2003.

[Holland, 1975] Holland, J.H.; *Adaptation in Natural and Artificial Systems*, The University of Michigan Press, 1975.

[Jackson & Carpenter, 2004] Jackson, B.; Carpenter, B.; *Optimal Placement of Spacecraft Sun Sensors Using Stochastic Optimization*, Proc. of IEEE Aerospace Conference, Vol.6, pg. 3916-3923, March 2004.

[Knapp & Carter, 1976] Knapp, C.; Carter, G.; The Generalized Correlation Method for Estimation of Time Delay, Proc. of IEEE Transactions on Acoustic, Speech, and Signal Processing, Vol. 24, No. 4, August 1976.

[Kuglin & Hines, 1975] Kuglin, C.D.; Hines, D.C.; *The Phase-correlation Imagine Alignment Method*, Proc. of Int. Conf. Cybernetics and Society, pg. 163-165, September 1975.

[Kulp, 1987] Kulp, D.; *Solar Maximum Mission Fine Pointing Sun Sensor Dawn and Dusk Errors, Flight Data and Model Analysis*, Computer Sciences Corporation, CSC/TM-87/6700, January 1987.

[Korepanov, 2003] Korepanov, V.E.; *The Modern Trends in Space Electromagnetic Instrumentation, Advances in Space Research*, Vol. 32, No. 3, pg. 401-406, 2003.

[Li & Yi, 2004] Li, M. H.; Yi, L. L.; *Accurate Direction-of-Arrival Estimation of Multiple Sources Using a Genetic Approach*, Wireless Communications and Mobile Computing, Vol.5, pg. 343-353, August 2005.

[Liebe et al, 1998] Liebe, C.C.; Dennison, E.W.; Hancock, B.; Stirbl, R.C.; Pain, B.; *Active Pixel Sensor (APS) based Star Tracker*, Proc. of IEEE Aerospace Applications Conference, Vol. 1, pg. 119-127, 1998.

[Liebe, 2002] Liebe, C.C.; Accuracy Performance of Star Trackers - A Tutorial, IEEE Transactions on Aerospace and Electronic Systems, Vol. 38, No. 2, April 2002.

[Liebe et al, 2002] Liebe, C.; Mobasser, S.; Bae, Y.; Wrigely, C.; Schroeder, J.; Howard, A.; *Micro Sun Sensor,* Proc. of IEEE Aerospace Conference, Vol. 5, pg. 2263-2273, March 2002.

[Li & Stoica, 1996] Li, J.; Stoica, P.; *Efficient Mixed-Spectrum Estimations with Applications to Target Feature Extraction*, IEEE Transactions on Signal Processing, Vol. 44, No. 2, February 1996.

[McNeil et al, 2003] McNeil, B.W.J.; Robb, G.R.M.; Poole, M.W.; *A Numerical Model of*

Electron Beam Shot Noise, Proc. of Particle Accelerator Conference, Vol.2, pg. 950-952, May 2003.

[National Aeronautics and Space Administration, 2005] National Aeronautics and Space Administration; *Total Ozone Mapping Spectrometer,* http://jwocky.gsfc.nasa.gov

[Oppenheim & Schafer, 1975] Oppenheim, A.; Schafer, R.; *Digital Signal Processing*, Englwood Cliffs, NJ: Prentice, 1975.

[Proakis & Manolakis, 1996] Proakis, J.G.; Manolakis, D.G.; *Digital Signal Processing - Principles, Algorithms, and Application*, Third Edition, Prentice Hall, 1996.

[Ryer, 1997] Ryer, A.; *Light Measurement Handbook*, International Light, 1997

[Stone, 1989] Stone, R.C.; *A Comparison of Digital Centering Algorithms*, The Astronomical Journal, Vol. 97, No. 4, pg. 1227-1237, 1989.

[Schmidt, 1986] Schmidt, R.D.; Multiple Emitter Location and Signal Parameter Estimation, IEEE Transactions on Antennas and Propagation, Vol. 34, pg. 276-280, March 1986.

[Tang et al, 1996] Tang, K.S; Man, K.F.; Kwong, S.; He, Q.; *Genetic Algorithms and their Applications*, IEEE Transactions on Signal Processing, Vol. 13, No. 6, Nov. 1996.

[Tang et al, 1994] Tang, K.S.; Man, K.F.; Chan, C.Y.; *Fuzzy Control of Water Pressure Using Genetic Algorithms*, IFAC Workshop on Safety, Reliability and Applications of Emerging Intelligent Control Technologies, pg. 15-20, Dec. 1994.

[Tlustos et al, 2003] Tlustos, L.; Davidson, D.; Campbell, M.; Heijne, E.; Mikulec, B.; *Fixed Pattern Deviations in Si Pixel Detectors Measure Using the Medipix1 Readout Chip*, Nuclear Instruments and Methods in Physics Research A 509, Elsevier Science B.V., pg. 102-108, 2003.

[Tsin et al, 2001] Tsin, Y.; Ramesh, V.; Kanade, T.; *Statistical Calibration of CCD Imaging Process*, Proc. of IEEE Int. Computer Vision Conference, pg. 480-487, 2001.

[Wertz, 2001] Wertz, J.; *Mission Geometry; Orbit and Constellation Design and Management*, Microcosm Inc. and Kluwer Academic Publishers, 2001.